This is the peer-reviewed, final accepted version for American Mineralogist, published by the Mineralogical Society of America.
The published version is subject to change. Cite as Authors (Year) Title. American Mineralogist, in press.
DOI: https://doi.org/10.2138/am-2025-9738. http://www.minsocam.org/

Revision 1

The partitioning of H between olivine and melt at low pressures (10 - 200 MPa)

----*Word Count:* 10742 (excludes title page, figures, references; all-inclusive: 15592)

Authors:

Liam D. Peterson[a,b,*], Megan E. Newcombe[b], Philip M. Piccoli[b], Austin Gion[c], Sune G. Nielsen[d], Glenn A. Gaetani[a], Adam R. Sarafian[e], Jianhua Wang[f]

Affiliations:

[a] Department of Geology and Geophysics, Woods Hole Oceanographic Institution, Woods Hole, MA 02540, United States

[b] Department of Geology, University of Maryland, College Park, MD 20742, United States

[c] Department of Earth Sciences, University of Oxford, Oxford OX1 3AN, United Kingdom

[d] CRPG, CNRS, Université de Lorraine, 15 rue Notre Dame des Pauvres, 54501 Vandoeuvre lès Nancy, France

[e]Corning Inc., Corning, NY 14873, United States

[f] Earth and Planets Laboratory, Carnegie Institution for Science, Washington, DC 20015, United States

_____

*Corresponding author: liam.peterson@whoi.edu

This is the peer-reviewed, final accepted version for American Mineralogist, published by the Mineralogical Society of America.
The published version is subject to change. Cite as Authors (Year) Title. American Mineralogist, in press.
DOI: https://doi.org/10.2138/am-2025-9738. http://www.minsocam.org/

Revision 1

20

21 **ABSTRACT**

22 The concentration of H_2O_T (i.e. total H; assumed here to be the sum of hydroxyl and
23 molecular water) in silicate minerals and melts exerts a primary control on the physicochemical
24 properties of Earth's crust and mantle. The partitioning of H_2O_T between minerals and melts is a
25 key parameter used to model the H_2O_T contents of magmatic source regions in terrestrial and
26 planetary systems. In mafic systems, olivine is frequently the first crystallizing phase, which
27 makes it a useful tracer of primitive melt composition. Previously, the partitioning of H_2O_T
28 between olivine and melt was only experimentally constrained at H_2O-undersaturated conditions
29 and pressures ≥ 500 MPa, which are broadly applicable to Earth's mid- to lower-crust and
30 uppermost mantle. However, we have few constraints at upper crustal pressures, limiting our
31 ability to model pre-eruptive H_2O_T contents, magma decompression rates, and ultimately
32 volcanic hazards. Here we present the first experimental determination of the partitioning of
33 H_2O_T between olivine and melt at pressures relevant to Earth's upper crust (10 – 200 MPa).
34 Contrary to predictions based upon extrapolation of experimental results from pressures ≥ 500
35 MPa, we find that the olivine-melt H_2O_T partition coefficient ($D_{H_2O_T}^{ol/melt}$= 0.0011 to 0.00033)
36 decreases with increasing melt H_2O_T and increasing pressure from 10 – 200 MPa. One
37 explanation for the observed relationship between $D_{H_2O_T}^{ol/melt}$ and melt H_2O_T concentration is that
38 $D_{H_2O_T}^{ol/melt}$ is controlled by the speciation of H (e.g., hydroxyl and molecular water) in silicate
39 melts. We calculate the concentration of hydroxyl (OH) dissolved in the melt, and assuming H is
40 only incorporated into olivine as OH, calculate an olivine-melt OH partition coefficient
41 ($D_{OH}^{Ol/melt}$). Our data indicate that $D_{OH}^{Ol/melt}$ is constant ($D_{OH}^{Ol/melt}$ = 0.0011±0.0002; 1 Std. Dev.)

and that the proportion of molecular water (H_2O_m) to OH in the melt controls the variation of $D_{H_2O_T}^{Ol/melt}$ with melt H_2O_T concentration for our experiments. We also compared San Carlos olivine seed crystals to olivine crystallized in the same experimental charges. Our data indicate that San Carlos olivine seed crystals have lower H_2O_T concentrations than olivine crystallized during the experiments, which may be explained by a difference in their compositions and therefore extrinsic point defect populations. Our results demonstrate that at low pressures (≤ 200 MPa) the partitioning of H_2O_T between olivine and melt is primarily dependent upon the speciation of H in silicate melts. Similarly, in combination with prior experimental work on clinopyroxene and plagioclase, our results suggest that the speciation of H in silicate melts may be a primary control on the partitioning of H_2O_T, at least at H_2O_T contents up to ~5 wt.%, between all nominally anhydrous minerals and melts. We apply our results to prior estimates for magma decompression rates from the 1977 fire fountain eruption at Seguam volcano and find that, for the variable $D_{H_2O_T}^{Ol/melt}$ determined in our study, median magma decompression rates are slightly slower (a factor of ~2.5) but within the uncertainty of models using a constant $D_{H_2O_T}^{ol/melt} =$ 0.0009±0.0003 (1 std. dev.; Towbin et al. 2023, *Am. Min.*). Therefore, prior estimates of magma decompression rates based upon H^+ diffusion in olivine may be slightly overestimated if the dependence of $D_{H_2O_T}^{ol/melt}$ on the speciation of H in the melt is unaccounted for.

Keywords: Olivine, Partitioning, Melt, Crust, Low Pressure

INTRODUCTION

This is the peer-reviewed, final accepted version for American Mineralogist, published by the Mineralogical Society of America.
The published version is subject to change. Cite as Authors (Year) Title. American Mineralogist, in press.
DOI: https://doi.org/10.2138/am-2025-9738. http://www.minsocam.org/

The total H (hereafter H_2O_T; assumed here to be the sum of hydroxyl and molecular water) contents of nominally anhydrous minerals (NAMs; e.g., olivine, pyroxene, feldspar) are increasingly being used as a tool to probe the H_2O_T contents of their magmatic source regions in terrestrial and planetary systems (e.g., Weis et al. 2015; Urann et al. 2022; Newcombe et al. 2023; Peterson et al. 2023b). Furthermore, diffusion-induced H_2O_T concentration profiles in NAMs have been used to constrain timescales of magmatic ascent in volcanic systems (e.g., Demouchy et al. 2006; Peslier and Luhr 2006; Ferriss et al. 2018; Newcombe et al. 2020). Accurate assessment of the H_2O_T content of primitive melts, and magma decompression rates, requires accurate determination of the partitioning of H_2O_T between the mineral and the melt, which can be described in terms of a partition coefficient:

$$D_{H_2O_T}^{min/melt} = \frac{C_{H_2O_T}^{min}}{C_{H_2O_T}^{melt}} \#(1)$$

where $D_{H_2O_T}^{min/melt}$ is the mineral-melt partition coefficient for H_2O_T between a mineral (min) and a melt ($melt$), $C_{H_2O_T}^{min}$ is the mass fraction of H_2O_T in a mineral, and $C_{H_2O_T}^{melt}$ is the mass fraction of H_2O_T in the coexisting melt.

In olivine, hydrogen is structurally incorporated as H^+ bound to O^{2-} anions at the apices of octahedral or tetrahedral sites to charge balance cation vacancies or substitutions (e.g., Kohlstedt and Mackwell 1998; Keppler and Bolfan-Casanova 2006; Tollan et al. 2017). In detail, H^+ may participate in single- and multi-site point structures (e.g., Berry et al. 2007; Tollan et al. 2018; Demouchy 2021) and can move through defect sites as single H^+ ions, regardless of the number of H^+ present in the defect site(s) (e.g., Ferriss et al. 2018; Jollands et al. 2019; Yang et al. 2019). Prior analytical and theoretical work suggests that the concentration of H^+ in a

This is the peer-reviewed, final accepted version for American Mineralogist, published by the Mineralogical Society of America.
The published version is subject to change. Cite as Authors (Year) Title. American Mineralogist, in press.
DOI: https://doi.org/10.2138/am-2025-9738. http://www.minsocam.org/

particular defect (e.g., metal vacancies) is dependent on the fugacity of H_2O (fH_2O; e.g., Tollan et al. 2017). To derive relationships between the concentration of H^+ in a particular defect and fH_2O, we make the simplifying assumption that two defects dominate the defect population of the grain and are present in equal proportions such that charge neutrality is maintained (i.e., a charge neutrality condition). For example, the charge neutrality condition defined by OH^- ions sitting in O-sites and vacancies in the metal (2^+ cation) sites can be written using Kröger-Vink notation (described in detail in Supplement S1) as:

$$[(OH_O^*)] = 2[V''_{Me}] \quad \#(2)$$

where [ ] brackets denote concentration, subscripts denote the defect site in the crystal structure, in this case *O* for the oxygen-site and *Me* for the metal-site, * denotes a positive charge relative to the typical charge of the defect site, and ′ denotes a negative charge relative to the typical charge of the defect site. A summary of relationships between the concentration of various H-bearing defects and fH_2O are given in Table 1. In short, H can be incorporated into the olivine structure through a large variety of defects and the concentration of H_2O_T in olivine is expected to be proportional to fH_2O^n ($n \approx 0.25 – 2$; Table 1).

Early works by Tomlinson (1956), Russell (1957), and Burnham and Davis (1974) argued that H_2O dissolves in silicate melt exclusively as OH based upon a linear relationship between the square root of H_2O_T concentration and fH_2O for pressures ≤ 1000 MPa. However, many subsequent works using infrared techniques have demonstrated the presence of dissolved H_2O_m (molecular H_2O) and OH in silicate glasses (Stolper 1982b; Newman et al. 1988; Silver and Stolper 1989). Building on this observation, speciation based models to describe the dissolution of H_2O in the melt as H_2O_m and OH species have been developed (e.g., Stolper 1982b, 1982a; Silver and Stolper 1985, 1989; Silver et al. 1990). At a given temperature and

This is the peer-reviewed, final accepted version for American Mineralogist, published by the Mineralogical Society of America.
The published version is subject to change. Cite as Authors (Year) Title. American Mineralogist, in press.
DOI: https://doi.org/10.2138/am-2025-9738. http://www.minsocam.org/

pressure, dissolution of H_2O into a silicate melt as H_2O_m or OH is proportional to fH_2O and $f_{H_2O}^{0.5}$, respectively (e.g., Zhang et al. 2007). Therefore, from a theoretical standpoint, the partition coefficient for H_2O_T between olivine and melt for a single H-bearing defect and charge neutrality condition in olivine can be written as:

$$D_{H_2O_T}^{ol/melt} = \frac{C_{Ol}^{OH}}{C_{melt}^{OH} + C_{melt}^{H_2O_m}} \propto \frac{af_{H_2O}^{n}}{b\sqrt{f_{H_2O}} + cf_{H_2O}} \quad \#(3)$$

where n ≈ 0.25 – 2 based upon the charge neutrality condition and H^+ incorporation mechanism (i.e., defect) in olivine (Table 1) and *a*, *b*, and *c* are constants for converting fugacity to concentration at a constant pressure and temperature. As the H_2O_T content of the melt increases, the proportion of dissolved OH in the melt relative to H_2O_m will decrease; as implied by Equation 3, this is expected to result in a variable $D_{H_2O_T}^{ol/melt}$.

The partitioning of H_2O_T between olivine and melt has been the subject of several experimental studies at lower crustal to upper mantle temperatures (T ≈ 1000 – 1450 °C), pressures (P ≈ 500 – 13000 MPa), and H_2O-undersaturated conditions (Koga et al. 2003; Aubaud et al. 2004; Hauri et al. 2006b; Grant et al. 2007; Tenner et al. 2009, 2012; O'Leary et al. 2010; Novella et al. 2014). Prior experimental studies were conducted at H_2O-undersaturated conditions and the fH_2Os of these experiments are poorly constrained, thereby preventing a direct evaluation of whether the theoretical relationship proposed above between $D_{H_2O_T}^{ol/melt}$ and fH_2O holds true.

Prior work suggests that $D_{H_2O_T}^{ol/melt}$ has a positive, linear dependence on pressure (Novella et al. 2014; Adam et al. 2016). This linear dependence is defined by a small number of experiments conducted at pressures of 6000 – 13000 MPa for which glass H_2O_T concentrations

are calculated via mass balance, which can be highly uncertain and critically relies on the assumption of negligible H loss during the experiments (Tenner et al. 2012; Novella et al. 2014). Furthermore, data from 500 – 2000 MPa exhibit significant scatter, which is greatly reduced when variations in analytical method are accounted for (Towbin et al. 2023); however, this also results in the removal of any resolvable pressure dependence from 500 – 2000 MPa (Towbin et al. 2023). The remaining scatter in $D_{H_2O_T}^{ol/melt}$ from 500 – 2000 MPa could be attributed to variations in fO_2, fH_2O, temperature, and melt or olivine composition, thereby obscuring any pressure dependence. We are currently unaware of any published experimental constraints on $D_{H_2O_T}^{ol/melt}$ at low pressures (≤ 500 MPa), which are relevant to Earth's upper crust, or at H_2O-saturated conditions. Constraining $D_{H_2O_T}^{ol/melt}$ at upper crustal pressures will allow us to more accurately model pre-eruptive volatile contents, magma decompression rates, and ultimately volcanic hazards associated with explosivity.

In this study, we present experimental $D_{H_2O_T}^{ol/melt}$ partitioning data from: 1) new analyses of prior experiments (Gaetani et al. 1994; Médard and Grove 2008); and, 2) newly conducted low pressure (20 – 100 MPa) experiments. New experiments were conducted on two natural starting materials, a basaltic-andesitic ash (MP; 2016 eruption of Mt. Pavlof, AK USA) and a primitive alumina-rich tholeiitic basalt (82-72f; primitive high-alumina basalt from Medicine Lake Volcano, CA, USA; See **Starting Materials**). Contrary to extrapolation from higher-pressure experimental data, we find that $D_{H_2O_T}^{ol/melt}$ is negatively correlated with pressure in our experiments. We evaluate this result in the context of crystal compositional controls (i.e., extrinsic defects), pressure, and the speciation of H in silicate melts and apply our results to a

prior estimate for the magma decompression rate of the 1977 fire fountain eruption at Seguam volcano.

EXPERIMENTAL DESIGN

Prior experiments

Several charges from the experiments of Gaetani et al. (1994) and Médard and Grove (2008) were analyzed as part of this study and are hereafter referred to as the "prior experiments". Experimental methods for the prior experiments are detailed elsewhere (Gaetani et al. 1994; Médard and Grove 2008) and summarized here. In brief, the experiments from Gaetani et al. (1994) were conducted at H_2O-saturated conditions, at the Ni-NiO (NNO) fO_2 buffer, and at 200 MPa on a natural basaltic-andesite starting material (Sample 135-839B-15R-2, 63-67 cm recovered during the Ocean Drilling Program) in TZM (titanium-zirconium-molybdenum) and MHC (molybdenum-hafnium-carbide) cold-seal pressure vessels. We subsequently analyzed charges #5 and #7 from Gaetani et al. (1994; hereafter G5 and G7). The experiments analyzed herein from Médard and Grove (2008) were conducted at H_2O-saturated conditions, at the NNO fO_2 buffer, and at pressures of 10 – 100 MPa on a primitive high-alumina basalt from Medicine Lake Volcano, CA (sample 82-72f; hereafter 82-72f; Donnelly-Nolan et al. 1991; Médard and Grove 2008) in MHC cold-seal pressure vessels. A subset of the experiments from Médard and Grove (2008) conducted at 10 and 25 MPa did not visually contain H_2O at the end of experimental runs and were not considered to be H_2O-saturated by the authors. We analyzed charges #7, #8, #11, and #23 from Médard and Grove (2008; hereafter M7, M8, M11, M23). Run conditions and phase compositions are compiled in Tables 2 and S2.

Starting materials

This is the peer-reviewed, final accepted version for American Mineralogist, published by the Mineralogical Society of America.
The published version is subject to change. Cite as Authors (Year) Title. American Mineralogist, in press.
DOI: https://doi.org/10.2138/am-2025-9738. http://www.minsocam.org/

For experiments performed as part of this work, the starting material was an olivine-rich basaltic-andesitic ash from the 2016 eruption of Mt. Pavlof, Alaska (hereafter MP; Table 2; Table 3; Rasmussen and Plank 2021). The MP starting material is enriched in SiO_2 relative to typical mafic arc magmas (Kovalenko et al. 2010), and is similar in composition to subduction-related high-Mg calc-alkaline andesites (Schmidt and Jagoutz 2017). The starting material was ground in an agate mortar and pestle and sieved to remove the < 90 μm, as well as the 106 to 180 μm fractions. Olivine grains were then picked from the 106 – 180 μm and >180 μm size fractions and used as seed grains for charges containing the MP starting material.

A subset of experiments was performed on a natural, primitive high-alumina basalt starting material (82-72f). This starting material was selected as it is identical to the 82-72f starting material from Medicine Lake Volcano used by Médard and Grove (2008) and is similar in composition to a low-pressure melt of a mantle lherzolite and a nominally primitive mid-ocean ridge basalt (Table 3; Bartels et al. 1991; Médard and Grove 2008). Furthermore, sample 82-72f has been the subject of several prior experimental studies (Bartels et al. 1991; Médard and Grove 2008; O'Leary et al. 2010; Mitchell et al. 2017).

Experimental methods

The new experiments reported in this study used a capsule-in-capsule approach to hold starting materials, buffer fO_2, and monitor fO_2 following the method of Alex and Zajacz (2020; Fig. 1). For sample capsules, ~10 mg of starting material was packed into a 6 mm long, 3 mm outer diameter (OD), 0.127 mm wall thickness (WT) $Au_{80}Pd_{20}$ capsule with ~5 mg H_2O (Table S1). For capsules containing the basaltic-andesite starting material, ~8 – 10 olivine grains picked from the 106 to 180 μm and the >180 μm size fractions were added as seeds (Table S1). For capsules containing the high-alumina basalt starting material, rectangular prisms of San Carlos

olivine ≤ ~1 mm in their longest dimension were added to the starting powder (Table S1). For fO_2 sensors, a 0.37 Co: 0.63 Pd powder mix was placed into a 7 mm long, 2.5 mm OD, 0.127 WT Pt capsule with a small piece of a fibrous Y-Zr sheet (hereafter Y-Zr paper) and ~3 mg H_2O and welded shut to prevent loss of material (Alex and Zajacz 2020). Sample capsules and fO_2 sensors were then loaded with 50 – 100 mg of Ni-NiO powder and 15 – 30 mg of H_2O (a ratio of 2 mg NNO: 1 mg H_2O) into 17 mm long, 5 mm OD, and 0.127 WT Pt outer capsules. All capsules were welded shut to limit loss of H_2O, weighed, heated in an oven at 120 °C for at least 12 hours, and then re-weighed to ensure capsules were fully sealed. We note that experiments XP-9, XP-10, and XP-13 contained two sample capsules, one with the basaltic-andesite starting material and one with the high-alumina basalt starting material. Experimental charges were then loaded into a sub-horizontal MHC cold-seal pressure vessel. The atmosphere inside the vessel was buffered to approximately the NNO fO_2 buffer by setting the partial pressure of H_2 in the system (Alex and Zajacz 2020). The vessel was then pressurized using Ar gas and final pressures were reached upon heating. All experiments were conducted at 1000 °C for 12 – 48 hr. Experiments were quenched by rotating the vessel-furnace assembly to a vertical position causing the charge to drop through a water-cooled collar and into the cool end of the vessel. Following quenching, capsules were re-weighed and then checked for leaks by submerging in acetone. Additionally, we attempted to visually confirm H_2O saturation through direct observation of H_2O liquid or gas upon opening sample capsules. In the event that capsules lost mass and H_2O was not visually confirmed, we texturally evaluated H_2O-saturation by checking for vesicles within experimental run products. Run conditions and evidence of H_2O-saturation are given in Table 2.

ANALYTICAL METHODS

This is the peer-reviewed, final accepted version for American Mineralogist, published by the Mineralogical Society of America.
The published version is subject to change. Cite as Authors (Year) Title. American Mineralogist, in press.
DOI: https://doi.org/10.2138/am-2025-9738. http://www.minsocam.org/

NanoSIMS analyses

Olivine analyses. Analyses of H_2O_T in olivine were conducted using the nanoSIMS 50L at the Carnegie Earth and Planets Laboratory (EPL) in Washington, DC. Analyses were conducted across three analytical sessions (MM/YY; 10/21, 08/22, 03/23). Analytical conditions, data processing procedures, and calibration curves for the 10/21 and 08/22 analytical sessions are detailed in Peterson et al. (2023a, 2023b). Olivine H_2O_T analyses were calibrated against a set of orthopyroxene standards from Kumamoto et al. (2017; BCN-203, DGO-160, SLP-403, SLP-108, PR-7-5, 109426), which generate a H_2O_T calibration curve within uncertainty of the olivine H_2O_T calibration curve (Kumamoto et al. 2017; Towbin et al. 2023). Calibration curves for orthopyroxene have been updated to match the revised values of Towbin et al. (2023). This results in a decrease of olivine H_2O_T concentrations by ~12 % and ~14 % for the 10/21 and 08/22 analytical sessions, respectively, relative to their original calibrations.

For the 03/23 analytical session, a ~2 nA Cs^+ primary beam was rastered over a 15×15 µm area for ~5 minutes to remove the Au coat and surface contamination. The raster size was then reduced to 10×10 µm and electronic gating and beam blanking were applied to focus ion collection from the central 5×5 µm portion of the raster and remove edge effects in the analytical signal. Counts of $^{12}C^-$, $^{16}O^1H^-$, $^{19}F^-$, $^{30}Si^-$, and $^{35}Cl^-$ ions were simultaneously detected on electron multipliers with a mass resolving power >8000 (MRP; Cameca definition), allowing for discrimination of $^{16}O^1H^-$ from $^{17}O^-$. For each analytical area, "heat" maps of ion counts were observed using the real-time imaging (RTI) function of the nanoSIMS 50L to check for sources of contamination such as cracks or resin. If hot spots, indicating likely sources of contamination, were identified using RTI, then the beam was moved to another location until a suitable analytical area was identified. Once a suitable analytical area was identified, the analytical area

was pre-sputtered for an additional 240 seconds prior to 250 seconds of counting time. The electron gun was used to charge compensate the sample surface due to implantation of Cs^+ ion from the primary beam and removal of negatively charged ions and electrons during analyses. Electron gun tuning followed protocols described in Peterson et al. (2023a). The vacuum in the analysis chamber was maintained at ~6.6×10^{-10} to ~9.2×10^{-10} torr.

Data reduction for the 03/23 analytical session followed protocols described in Peterson et al. (2023a). The effects of instrumental drift due to variation in analytical conditions (e.g., instability of the primary beam and electron gun, variations in detector efficiency and vacuum pressure) were accounted for by normalizing counts of volatile ions (e.g., $^{12}C^-$, $^{16}O^1H^-$, $^{35}Cl^-$) to $^{30}Si^-$, which effectively smooths these net effects. All data were then normalized to a factor of $SiO_2/50$, where SiO_2 is the wt. % SiO_2 of the target as measured by EPMA (Hauri et al. 2002; Shimizu et al. 2022; Towbin et al. 2023; Peterson et al. 2024). The multiplication of $^{16}O^1H/^{30}Si$ by $SiO_2/50$ assumes an approximately linear response between the SiO_2 content of the target phase and counts of ^{30}Si, which may introduce some uncertainty. We note that normalization of $^{16}O^1H$ counts to ^{30}Si and multiplication by $SiO_2/50$ has been shown to improve agreement amongst compositionally-diverse (e.g., basalt, rhyolite, SiO_2 glasses), single phase (e.g., glass, pyroxene) calibration curves for H_2O_T (Aubaud et al. 2007; Mosenfelder and Rossman 2013; Shimizu et al. 2022). The analytical background for $OH/Si\times SiO_2/50$ was monitored using repeat analyses of Suprasil 3002 glass (~1.7±0.6 μg/g H_2O_T; Newcombe 2022; Peterson et al. 2023a) held in the sample mount, as well as essentially anhydrous, synthetic forsterite (SynFo; <<1 μg/g H_2O_T) held in the standard mounts. A correction to the $OH/Si\times SiO_2/50$ of Suprasil 3002 glass to account for dissolved H was made following protocols described in Peterson et al. (2023b, 2023a) to determine the analytical background. Over the entire analytical session, repeat analyses

of ALV-519-4-1 (~1700 µg/g H_2O_T) and Herasil glass (~80 – 100 µg/g H_2O_T) show no systematic variation in OH/Si×SiO_2/50 (Fig. S1). Therefore, we elect not to apply drift corrections to data from the 03/23 analytical session. Measurements of H_2O_T in olivine were calibrated using an orthopyroxene calibration curve, which has been demonstrated to be within the analytical precision of the olivine calibration curve (Kumamoto et al. 2017; Towbin et al. 2023). The fitting procedure for calibration curves follows protocols detailed in Peterson et al. (2023a), and calibration standards and calibration curves are reported in the supplement (Table S3; Fig. S8). Data were filtered for outliers in C and Cl, which are highly incompatible in olivine, and are considered here as indices of contamination.

Glass analyses. Silicate glass from experimental run products, as well as one glassy melt inclusion from an olivine grain in the MP starting material were analyzed for H_2O_T using the NanoSIMS 50L at Carnegie EPL. Analyses were conducted in imaging mode on the NanoSIMS 50L across two sessions, 08/22 and 03/23, and followed the method outlined in Peterson et al. (2023b). For both analytical sessions, analyses were conducted using entrance slit 5 and aperture slit 4, and a beam current of ~200 pA. A 15 ×15 µm area was pre-sputtered for 4 minutes using a 2 nA Cs^+ primary beam prior to analyses to remove the Au coat and surface contamination. The analytical area was then decreased to 10 ×10 µm and pre-sputtered for an additional 3 minutes using a 200 pA Cs^+ primary beam. Analyses were conducted using a 128 × 128 pixel working frame with 200 cycles over 670 seconds. A MRP (Cameca definition) of >8000 was used such that $^{16}O^1H^-$ could be discriminated from $^{17}O^-$. Beam-blanking was not applied; however, corresponding analytical effects (e.g., edge effects from SIMS pits) were removed in post-processing. The vacuum in the analysis chamber was maintained at ~9×10^{-10} torr and 9.1×10^{-10} to 8.6×10^{-10} torr for the 08/22 and 03/23 analytical sessions, respectively.

This is the peer-reviewed, final accepted version for American Mineralogist, published by the Mineralogical Society of America.
The published version is subject to change. Cite as Authors (Year) Title. American Mineralogist, in press.
DOI: https://doi.org/10.2138/am-2025-9738. http://www.minsocam.org/

Images were analyzed and post-processed following procedures outlined in Peterson et al. (2023b) and Shimizu et al. (2021). As for olivine analyses, analyses of volatile ions (e.g., $^{12}C^-$, $^{16}O^1H^-$, $^{35}Cl^-$) were ratioed to $^{30}Si^-$ and normalized to $SiO_2/50$, where SiO_2 is the wt. % SiO_2 of the target as measured by EPMA. For samples B-09 and B-10, glass major element data was unable to be collected due to loss of material during removal of the Au coat, therefore a SiO_2 content of 60±9 wt. % was assumed based upon the measured glass SiO_2 from sample B-13 and the range in SiO_2 contents present in MP charges (Table S2). Analyses were calibrated against a set of basaltic glass standards (ALV-519-4-1, D52-5, D30-1; Hauri et al. 2002, 2006a) in addition to Suprasil 3002 glass, which was used as a blank material due to its exceptionally low H_2O_T concentration (~1.7±0.6 µg/g H_2O_T; 1 std. dev.; Newcombe 2022) relative to unknowns (~0.2 – 4.5 wt. % H_2O_T; Table 4). Calibration curves are provided in Fig. S9 and S10. We assign a conservative estimate of ±10% uncertainty to the calibration curves for all elements based upon the long-term reproducibility of the glass standards (Hauri et al. 2002). For H_2O_T, we note that the estimated ±10% uncertainty is most applicable to materials with H_2O_T concentrations below ~3 wt.% and that calibration curves may become increasingly non-linear at high H_2O_T concentrations (e.g., Hauri et al. 2002; Moussallam et al. 2024) The measured H_2O_T concentration for Suprasil 3002 glass was ~5 µg/g H_2O_T for the 08/22 analytical session and varied from ~270 to ~30 µg/g H_2O_T during the 03/23 analytical session. No blank corrections were applied as the measured H_2O_T of Suprasil 3002 glass is lower than the analytical uncertainty in non-blank corrected data. As for olivine, data are filtered based upon C and Cl, with analyses with ≥100 µg/g CO_2 (total C quantified as CO_2) and order of magnitude outliers for Cl being removed. The unprocessed and filtered datasets are presented in Supplementary Tables S6, S7, and S10.

Analyses of prior experiments. Analyses of H_2O_T were conducted using the Cameca NanoSIMS 50L at the Carnegie EPL. Analyses were conducted in 2017 and followed previously published methods (Hauri et al. 2002; Koga et al. 2003; A. R. Sarafian et al. 2017). Briefly, olivine and glass analyses were conducted using a primary beam current of 5 nA and 1 nA, respectively. For all analyses, a 15×15 μm area was pre-sputtered, prior to decreasing the analytical areas to 5×5 μm and 10×10 μm for olivine and glass, respectively. Counts of ^{12}C, $^{16}O^{1}H$, ^{19}F, ^{30}Si, and ^{35}Cl, and ^{30}Si were simultaneously detected on electron multipliers. A MRP (Cameca definition) >8000 was used, which allows for discrimination of $^{16}O^{1}H^{-}$ from $^{17}O^{-}$. Suprasil 3002 glass (1.7±0.6 μg/g H_2O_T; 1 std. dev.; Newcombe 2022; Peterson et al. 2023a), Herasil 102 glass (~80 μg/g H_2O_T), and ALV-519-4-1 (1700 μg/g H_2O_T) were used as reference materials and were regularly analyzed throughout the analytical session to monitor instrumental drift and the analytical background. Reference materials were reanalyzed before and after changing beam currents to ensure calibrations were not affected by modification of the beam current. Blank corrections were applied to all data, except calibration curves for which blank materials were not analyzed, by subtracting the average $OH/Si \times SiO_2/50$ of Suprasil 3002 glass analyses that bracketed unknowns. An additional correction to account for dissolved H in Suprasil 3002 glass was applied to blank estimates as in Peterson et al. (2023b). If this correction is not made, all reported concentrations are decreased by ~1.7 μg/g H_2O_T, this results in a < 10% decrease in H_2O_T concentrations in olivine and no change for the reported H_2O_T of silicate glass. Drift corrections were only applied to data from hours ~50 – 64 after the start of the analytical session, as the $OH/Si \times SiO_2/50$ of ALV-519-4-1 was invariant outside this window. Drift corrections followed the same time variant approach used in Peterson et al. (2023a, 2024). Analyses of H_2O_T in olivine were calibrated against olivine standards: CMOL58, GRR1012, and

ROM177. Analyses of H_2O_T in glass were calibrated against glass standards: 1654, 1833-11, 1833-1, 1846-12, ALV-519-4-1, and WOK 28-3. Data filtering for olivine and glass analyses followed the same method as above. Standard values, calibration curves, and citations for standards are provided in the supplement (Table S3, Fig. S11).

EPMA analyses

Olivine and glass analyses for new experiments. The major and minor element compositions of olivine and glass were measured by using the JEOL JXA 8900R electron probe microanalyzer (EPMA) at the University of Maryland – College Park (UMD) following the methods of Peterson et al. (2023b, 2024). Depending upon the amount of suitable analytical area, one to three EPMA analyses were conducted around each SIMS pit. Data processing criteria for EPMA data are detailed in Supplement S2. Phase compositions are reported in Table S2.

Olivine analyses for prior experiments. Major and minor element concentrations of the olivine were measured for the experiments of Gaetani et al. (1994) and Médard and Grove (2008) by using the JEOL JXA-8200 electron probe at the Massachusetts Institute of Technology. A 50 nA beam current and 15 kV accelerating voltage was used. We counted on peak for 400 s for TiO_2, Al_2O_3, and FeO and 40 s for SiO_2, Cr_2O_3, MnO, MgO, CaO, and P_2O_5. Analyses were calibrated against internal standards (synthetic fayalite, synthetic forsterite, and olivine P-140). Phase compositions are reported in Table S2.

RESULTS

Run products

All run products contained quench-growth-free glass, olivine, and plagioclase. Run products from charges containing the MP starting material contain small (< a few μm), highly

reflective, opaque grains that are likely Fe-Ti-oxides. Olivine grains are frequently subhedral, but some are euhedral with an angular and blocky appearance (Fig. 2). Olivine grains from charges containing the MP starting material are predominantly < 100 μm diameter on their long axis. Angular, elongated olivine grains are likely remnants from the crushed starting material, whereas subhedral to euhedral olivine grains may represent new grain growth. Rare olivine grains >150 μm in diameter found in MP-07, MP-10, MP-14, and MP-17 are anhedral to euhedral, contain melt inclusions or melt embayments, and represent large seed crystals from the MP starting material (see **Experimental Design**). Olivine grains in the run products of the basaltic starting material are predominantly subhedral, with rare euhedral grains, and are < ~150 μm on their long axis. Olivine grains in charges containing the basaltic starting material are likely the product of grain growth as the starting material was a fine powder with a grain size <<100 μm. For all charges (excluding the "prior experiments"), glassy melt pools are <10 μm, except for MP-05 which has large melt pools (>75 μm). Mass balance calculations were not performed for the newly conducted experiments due to the inclusion of seed crystals in all charges and the relatively low temperature of the experiments (1000 °C) which likely did not cross the liquidus of the starting materials (Médard and Grove 2008). Regardless, for the duration (24 hr.), temperature (1000 °C), and oxygen fugacity (NNO) of the newly conducted experiments, we expect Fe-loss to capsule materials to be minimal (Hall et al. 2004).

H_2O saturation in new experiments

All run products for newly conducted experiments contain roughly spherical to elongate voids interpreted as vesicles (Supplementary data file "Sample_Maps.zip"), suggesting that a fluid phase, likely H_2O vapor, was present when experiments were quenched. Water or water vapor were visually identified in the outer capsule of XP-03, and the inner capsules MP-09, B-

09, MP-13 and B-13 upon opening confirming the presence of a hydrous fluid phase over the duration of the experiments (Table 2). Additionally, the nested capsule assemblies for charges MP-02 and MP-13/B-13 experienced no mass loss during the experimental run, suggesting no or minimal H loss occurred. Overall, we were able to visually confirm H_2O-saturation in several charges and argue that the remaining charges were H_2O-saturated based upon experimental (i.e., mass loss) and textural (i.e., vesicularity) arguments.

Equilibrium, disequilibrium, or metastable equilibrium in new experiments

At the temperatures of our experiments, H^+ diffusion in olivine is rate-limited by diffusion of metal vacancies. We calculate equilibration timescales for olivine in our run products following the method detailed in E. Sarafian et al. (2017). In short, we generate an analytical solution for H^+ diffusion and equilibration in a spherical olivine using the formulation for non-steady state diffusion through a sphere with a constant surface concentration from Crank (1979). We consider two model set-ups relevant to equilibration of the largest non-San Carlos seed crystal in our run products and the San Carlos olivine seed crystals, respectively. Model parameters are summarized in Table S11. We calculate equilibration times of ~15 hr. for non-San Carlos seed crystals and ~59 hr. for San Carlos olivine seed crystals, which exceeds the maximum duration of our experiments (48 hr.), therefore we may expect to observe gradients with respect to H_2O_T in San Carlos olivine seed crystals. However, no such gradients were observed in San Carlos olivine seed crystals (Fig. S12 – S18), potentially suggesting the crystals may be at a metastable equilibrium with respect to H_2O_T (see **Extrinsic defects**). For charges containing the MP starting materials, SIMS transects preferentially target seed grains due to their large size (> 100 μm; Fig. S21) relative to grains that may have grown during our experiments (e.g., Fig. S22). Transects in MP run product olivine grains are predominantly heterogeneous

This is the peer-reviewed, final accepted version for American Mineralogist, published by the Mineralogical Society of America.
The published version is subject to change. Cite as Authors (Year) Title. American Mineralogist, in press.
DOI: https://doi.org/10.2138/am-2025-9738. http://www.minsocam.org/

(Fig. S20, S21, S23, S24, S25), either due to incomplete equilibration, metastable equilibrium of H-bearing defects, or local re-equilibration of olivine H_2O_T concentrations due to concealed melt inclusions (Fig. S22; Mutch et al. 2024). Due to the prevalence of heterogeneous transects, ambiguity in assignment of growth vs. seed grains due to sample preparation (e.g., starting material grain size <90 μm; see **Starting materials**), and the overall scatter in the H_2O_T data, we elect to treat all MP olivine grains as seed grains that have reached metastable equilibrium for H_2O_T (see **Extrinsic defects**). For olivine grains from charges containing the basaltic starting material, equilibrium is likely as grains were grown during the experiments. Time-series experiments were run at intervals of 12, 24, and 48 hr. (Fig. 3). For the basaltic starting material, olivine H_2O_T concentration, melt H_2O_T concentration, and $D_{H_2O_T}^{ol/melt}$ are scattered, but within uncertainty of each other, whereas for the MP starting material glass H_2O_T concentration decreases and $D_{H_2O_T}^{ol/melt}$ increases with time (Fig. 3). Overall, we suggest that run products from our basaltic starting material likely represent equilibrium, whereas run products from the MP starting material and San Carlos olivine seed grains are more likely to preserve signatures of metastable equilibrium.

Hydrogen solubility in olivine

We measured H_2O_T concentrations in olivine grains from 6 prior experiments and 17 new experiments, including 5 San Carlos olivine seed crystals from charges containing the basaltic starting material (i.e., 82-72f). The majority of olivine grains from MP run products have H_2O_T concentrations that overlap within measurement uncertainty. Olivine grains from MP run products have distinctly higher H_2O_T concentrations in experiments conducted at 100 MPa than those at 50 MPa or olivine grains from the MP starting material (MP starting material: 13±3 μg/g

418 H_2O_T; 1 std. dev.; Fig. 4). Across our dataset, we find no correlation between olivine H_2O_T and
419 major and trace element concentrations (as measured by EPMA). We fit power laws to the
420 relationships between olivine H_2O_T with pressure, fH_2O, and glass H_2O_T concentrations for
421 experiments B-09, B-10, G5, G7, M7, and M8 which contain grown olivine grains, which are
422 expected to be equilibrated for H as well as major and trace elements (hereon the "fully
423 equilibrated experiments"), and were conducted at H_2O-saturated conditions (Table 2, Table 4,
424 Fig. 5). Data for all other experiments analyzed in this study are included in Fig. 5 for reference.
425 We note that H_2O_T concentrations for all non-San Carlos olivine seed crystals follow the power
426 law regressions regressed through the fully equilibrated experiments with some scatter (Fig. 5).

427 **Hydrogen solubility in basaltic and basaltic-andesite glass**

428 We measured the H_2O_T concentration of glasses in run products of the MP and basaltic
429 starting materials as well as prior experiments (Table 4). We fit power laws to the relationships
430 between glass H_2O_T, pressure, and fH_2O for experiments MP-03, MP-09, MP-10, B-09, B-10,
431 G5, G7, M7, and M8 which were visually confirmed to be H_2O-saturated (Table 2; Fig. 6a, b).
432 For our 100 MPa experiments on the MP starting material, glass H_2O_T concentrations are
433 negatively correlated with alkalis ($Na_2O + K_2O$; Fig. 6c), although this trend is anchored by a
434 single data point. We find that glass H_2O_T concentrations do not correlate with other
435 compositional parameters constrained in our data set.

436 **Comparison to existing H_2O_T solubility models.** Several prior studies have examined
437 the solubility of H_2O_T in basaltic to rhyolitic melts and developed corresponding H_2O_T solubility
438 models (Moore et al. 1998; Pineau et al. 1998; Newman and Lowenstern 2002; Iacovino et al.
439 2021). The H_2O_T contents of glasses generated from the basaltic starting material at 100 MPa,
440 1000 °C, and at the NNO fugacity buffer are in good agreement with H_2O_T solubility models for

441 basaltic melts (Table 4; Moore et al. 1998; Newman and Lowenstern 2002). Conversely, the
442 H_2O_T contents of glasses generated from the MP starting material are in poor agreement with
443 prior studies of H_2O_T solubility in basaltic-andesitic melts (Table 4; Moore et al. 1998; Pineau et
444 al. 1998). It is unlikely that the disagreement between the measured and predicted H_2O_T
445 solubility of glasses in MP run products represents an analytical effect as glass H_2O_T contents are
446 consistent within a charge, between charges, and across analytical sessions. We present our
447 measured glass H_2O_T contents and predicted glass H_2O_T contents using the model of Moore et al.
448 (1998) in Table 4, but only consider our measured glass H_2O_T contents for the remaining
449 discussion.

450 **Olivine-melt partitioning**

451 We use our measured olivine and glass H_2O_T contents to calculate $D_{H_2O_T}^{ol/melt}$ (Table 4). At
452 100 MPa, we find no resolvable difference in $D_{H_2O_T}^{ol/melt}$ between run products from our MP and
453 basaltic starting materials. Conversely, $D_{H_2O_T}^{ol/melt}$ calculated from San Carlos olivine seed grains
454 held in charges B-10 and B-13 are resolvably lower than all other experiments at 100 MPa (Fig.
455 7a). We find that $D_{H_2O_T}^{ol/melt}$ decreases with increasing pressure, fH$_2$O, and glass H_2O_T
456 concentrations (Fig. 7). The decrease of $D_{H_2O_T}^{ol/melt}$ with increasing pressure for our experiments is
457 contrary to the positive, linear relation previously identified for experiments from 500 – 13000
458 MPa (Tenner et al. 2009; Adam et al. 2016). Our data from 10 – 85 MPa are broadly
459 unresolvable from the preferred $D_{H_2O_T}^{ol/melt}$ value at 500 – 2000 MPa determined by Towbin et al.
460 ($D_{H_2O_T}^{ol/melt}$ = 0.0009±0.0003; 1 std. dev.; 2023), although nearly all data from 100 – 200 MPa have
461 central values that fall outside this range (Table 4; Fig. 7a). For experiments in which olivine is

fully equilibrated and that were visually confirmed to be H_2O-saturated (i.e., B-09, B-10, G5, G7, M7, M8), we elect to fit a linear exponential loss (LINEX) function to the relationships between $D_{H_2O_T}^{ol/melt}$, fH_2O and glass H_2O_T (Fig. 7). A LINEX function is a linear combination of a linear and exponential function and yields an approximation of an asymmetric quadratic function. A function of this form does not have a vertical asymptote inherent to power laws with negative exponents, thereby approximating the behavior of a function with a y-intercept as x approaches zero. This is preferable due to the dependence of $D_{H_2O_T}^{ol/melt}$ on the speciation of H in the melt and fH_2O (eq. 3; see **The effect of hydrogen speciation in the melt**). We note that the empirical fits presented in Fig. 7 are only valid over the conditions of our experiments and further extrapolation may produce unrealistic results and should be treated with extreme caution (e.g., Fig. S4).

San Carlos seed grains

Center to edge transects were measured in grains and grain fragments of San Carlos olivine seeds included in experiments containing the basaltic starting material. For all charges, except B-10, quenching and distortion of capsules during disassembly caused the San Carlos olivine seed grains to become disaggregated from all other run products. Due to the friability of the basaltic run products, removal, polishing, and mounting of materials proved difficult and resulted in limited availability of materials from the basaltic charges. We recovered and analyzed San Carlos seeds from charges B-07, B-10, B-13, and B-14. The H_2O_T of San Carlos seed grains are variable between charges (2.6±0.1 – 10.7±0.5 μg/g H_2O_T; 1 std. dev.), and only the San Carlos seed from charge B-14 (2.6±0.1 μg/g H_2O_T; 1 std. dev.) is indistinguishable from the San Carlos olivine starting material (2.3±0.3 μg/g H_2O_T; 1 std. dev.). The H_2O_T contents of San

This is the peer-reviewed, final accepted version for American Mineralogist, published by the Mineralogical Society of America.
The published version is subject to change. Cite as Authors (Year) Title. American Mineralogist, in press.
DOI: https://doi.org/10.2138/am-2025-9738. http://www.minsocam.org/

Carlos olivine seeds are weakly pressure dependent (Fig. S2) and do not correlate with any trace element concentrations measured herein (e.g., Ca, Ti, Na) consistent with prior work on natural olivines (e.g., Demouchy and Alard 2021). Paired San Carlos olivine seed grains and olivine grains crystallized during the experiments (hereafter "grown olivine") were measured in the run products of charges B-10 and B-13. We find that the H_2O_T contents of grown olivine grains from charges B-10 (20±4 µg/g H_2O_T; 1 std. dev.) and B-13 (23±7 µg/g H_2O_T; 1 std. dev.) are distinctly higher than their corresponding San Carlos seeds (5.4±0.5 µg/g H_2O_T and 10.7±0.5 µg/g H_2O_T, respectively; 1 std. dev.).

DISCUSSION

Our findings demonstrate that $D_{H_2O_T}^{ol/melt}$ decreases with increasing pressure from 10 – 200 MPa, contrary to the linearly increasing trend predicted by fits to data from higher pressure (≥ 500 MPa) experiments (Tenner et al. 2012; Novella et al. 2014; Adam et al. 2016). The distinct decrease of $D_{H_2O_T}^{ol/melt}$ over our experimental pressure range (10 – 200 MPa) may primarily be a function of pressure; however, it is possible that this deviation from the expected trend is related to crystal compositional controls (e.g., compositionally related crystal defects) or changes in $f$$H_2O$ and the speciation of H in silicate melts. We explore the roles of extrinsic point defects (i.e., those defects associated with trace element impurities) and the speciation of H in silicate melts below.

Extrinsic point defects

The equilibrium extrinsic point defect concentration of an olivine is set by the olivine composition, which is in turn controlled by the composition of the last melt with which the olivine fully equilibrated for all elements. For the newly conducted experiments, the major and

This is the peer-reviewed, final accepted version for American Mineralogist, published by the Mineralogical Society of America.
The published version is subject to change. Cite as Authors (Year) Title. American Mineralogist, in press.
DOI: https://doi.org/10.2138/am-2025-9738. http://www.minsocam.org/

trace element contents of seed olivine grains are unable to undergo complete diffusive equilibration for major and trace elements due to the short run durations (<48 hr.) and low temperature (1000 °C). Therefore, the extrinsic point defect concentration of seed grains will be set by their source magmas whereas the defect population of grown olivine grains will be set by the experimental melts. A first-order evaluation of the dependence of olivine H_2O_T concentrations on the point defect population of the grains can be obtained by comparing olivine H_2O_T concentrations with major (i.e., Fe, Mg, Ca, Mn) and trace element (i.e., Ti, Al, Na, K, Ni) concentrations. Within the resolution of our measurements and the subset of elements analyzed herein, we found no correlations between olivine H_2O_T and major or trace element concentrations for all non-San Carlos olivine grains. This suggests that the total concentration of extrinsic point defects (i.e., the sum of all extrinsic defects) is not the dominant control on H_2O_T solubility in olivine for our experiments. However, we note that San Carlos olivine seed grains have lower H_2O_T concentrations than olivine grains from the same charge (Fig. 8; see "**San Carlos seed grains**") and have lower Ca concentrations (≤0.08 wt.% CaO vs. ~0.2 – 0.4 wt.% CaO) and higher Fo contents (Fo91 vs. ~Fo67 – Fo89) than other run product olivine grains studied herein (Table 4; Table S2). This observation is consistent with prior work that indicates H_2O_T solubility in olivine increases with the Fe and trace element contents (e.g., Zhao et al. 2004; Berry et al. 2007; Tollan et al. 2018). Taken together, this implies that the composition, which sets the defect concentration of the olivine, exerts some control on H_2O_T solubility over a broad compositional space.

Next, it is useful to consider the conditions under which seed grains were last equilibrated for major and trace elements. The San Carlos olivine seed grains last equilibrated their major and trace elements at nearly anhydrous conditions (~50 – 200 μg/g H_2O_T in the source; Li et al. 2008)

whereas seed grains from the MP starting material likely equilibrated their major and trace elements with melts containing several wt. % of H_2O_T, similar to other lavas from the Aleutian arc (e.g., Zimmer et al. 2010). Similarly, olivine grains grown during our experiments equilibrated their major and trace elements with melts containing several wt. % of H_2O_T (Table 4). In the case of the San Carlos olivine seed grains, equilibration of point defects at nearly anhydrous conditions would have resulted in the formation of stable anhydrous point defects which may present an energetic barrier to H incorporation during our experiments. Under this scenario, anhydrous defects remain metastable until an energetic threshold is crossed resulting in reconfiguration of defect sites in the crystal lattice and/or paired diffusion of major and trace elements and associated defects. Similarly, it is possible that the reconfiguration and availability of point defects that can incorporate H^+ is rate limited by the sluggish kinetics (i.e., slow diffusion) of major and trace element diffusion, relative to H^+, in olivine (e.g., Costa et al. 2020). A "sluggish kinetic" effect has been observed during the simultaneous dehydration of multiple plagioclase grains of differing compositions, which plateaued to different values after ~30 hr. and converged to one value after ~900 hr. (Behrens 2021). Without direct constraints on the distribution of point defects and zonation of major and trace elements for seed grains before and after experimental runs, we cannot distinguish between the metastable equilibrium and sluggish kinetics scenarios. Due to this, we consider the metastable equilibrium and sluggish kinetics scenarios to fall under the umbrella of "seed effects", which reflect a pre-existing control on the point defect chemistry of the grains set by complete equilibration of their point defect chemistries with a chemical system that is distinct from the experimental system. We may expect to observe a "seed effect" in olivine grains from our MP run products; however, they are likely to be less pronounced as MP olivine seed grains are less than a few hundred μm in their long axis

This is the peer-reviewed, final accepted version for American Mineralogist, published by the Mineralogical Society of America.
The published version is subject to change. Cite as Authors (Year) Title. American Mineralogist, in press.
DOI: https://doi.org/10.2138/am-2025-9738. http://www.minsocam.org/

552 (relative to ~1 mm for San Carlos olivine seeds) and likely equilibrated with a hydrous magma
553 (e.g., Zimmer et al. 2010). Nevertheless, it is possible that a "seed effect" is responsible for some
554 or all of the scatter observed in our MP run product olivine data. Further experimental work
555 examining the hydration of essentially anhydrous olivine grains generated by thermal annealing
556 and complete equilibration with an anhydrous melt should be undertaken to evaluate the "seed
557 effect" hypothesis.

558 From a H_2O_T partitioning standpoint, we interpret the lower $D_{H_2O_T}^{ol/melt}$ values from San
559 Carlos olivine seed grains in run products from B-09 and B-10 to reflect a "seed effect" as
560 discussed above. Curiously, the $D_{H_2O_T}^{ol/melt}$ values derived from San Carlos olivine seed grains fall
561 close to the linear trend defined by all high pressure experimental data (Fig. 7a), although this
562 may simply be serendipitous as olivine compositions and the degree of H_2O-undersaturation
563 varies across all high pressure experiments rendering them difficult to compare (Koga et al.
564 2003; Aubaud et al. 2004; Hauri et al. 2006b; Grant et al. 2007; Tenner et al. 2009, 2012;
565 O'Leary et al. 2010; Novella et al. 2014). Therefore, we elect to exclude $D_{H_2O_T}^{ol/melt}$ data from San
566 Carlos olivine seed grains from further evaluation of the controls on $D_{H_2O_T}^{ol/melt}$. Similarly, we elect
567 to exclude $D_{H_2O_T}^{ol/melt}$ data from our MP run products due to the potential for "seed effects" as
568 observed for San Carlos olivine seed grains. We note that the $D_{H_2O_T}^{ol/melt}$ values derived from MP
569 run products follow the trends defined by experiments for which olivine is in equilibrium with
570 the experimental melt (i.e., B-09, B-10, G5, G7, M7, and M8) albeit with some scatter. Overall,
571 our results imply that the concentration and/or the metastable equilibrium of (an)hydrous defects
572 in olivine may exert a significant control on $D_{H_2O_T}^{ol/melt}$ for experimental or natural systems in
573 which olivine grains are incompletely equilibrated for, at least, major defect forming elements.

This is the peer-reviewed, final accepted version for American Mineralogist, published by the Mineralogical Society of America.
The published version is subject to change. Cite as Authors (Year) Title. American Mineralogist, in press.
DOI: https://doi.org/10.2138/am-2025-9738. http://www.minsocam.org/

574 **Is pressure the primary control on olivine-melt hydrogen partitioning at all conditions?**

575 Prior experimental work has suggested that $D_{H_2O_T}^{ol/melt}$ increases linearly with pressure at
576 500 – 13000 MPa (Tenner et al. 2012; Novella et al. 2014; Adam et al. 2016). A recent study by
577 Towbin et al. (2023) demonstrated that once variability in analytical methods is accounted for,
578 $D_{H_2O_T}^{ol/melt}$ values from experiments at 500 – 2000 MPa have no resolvable variation with pressure
579 ($D_{H_2O_T}^{ol/melt} = 0.0009 \pm 0.0003$; 1 std. dev.). Considering these results separately and extending
580 them to our experimental pressure range, it is expected that $D_{H_2O_T}^{ol/melt}$ would be positively
581 correlated or invariant with pressure. However, we observe a resolvable decrease in $D_{H_2O_T}^{ol/melt}$
582 from 10 to 200 MPa, contrary to extrapolations from higher pressure data (Fig. 7a). The change
583 in functional form (linear vs. exponential) and slope of correlation (e.g., positive or negative) for
584 $D_{H_2O_T}^{ol/melt}$ with pressure is consistent with a change in the dominant mechanism(s) controlling
585 $D_{H_2O_T}^{ol/melt}$ at the conditions of our experiments. An inter-comparison of $D_{H_2O_T}^{ol/melt}$ with glass and
586 olivine H_2O_T concentrations shows that $D_{H_2O_T}^{ol/melt}$ is correlated with glass H_2O_T (R^2=0.63) and
587 uncorrelated with olivine H_2O_T (R^2=0.078) concentrations (Fig. S3) implying that variations in
588 the melt exert a greater control on $D_{H_2O_T}^{ol/melt}$ for our experiments. We explore the role of H
589 speciation in the melt, which is inter-related to fH_2O, in controlling $D_{H_2O_T}^{ol/melt}$ in the following
590 section.

591 **The effect of hydrogen speciation in the melt**

592 Previous work has shown that, on a single oxygen basis, the mole fraction of OH in
593 silicate melts is proportional to $\sqrt{f_{H_2O}}$ and the mole fraction of H_2O_m is proportional to fH_2O,

This is the peer-reviewed, final accepted version for American Mineralogist, published by the Mineralogical Society of America.
The published version is subject to change. Cite as Authors (Year) Title. American Mineralogist, in press.
DOI: https://doi.org/10.2138/am-2025-9738. http://www.minsocam.org/

which is consistent with infrared spectroscopic measurements of OH^- and H_2O_m in silicate glasses (Stolper 1982a; Silver and Stolper 1985, 1989; Silver et al. 1990; Newcombe et al. 2017). Furthermore, speciation-based models of H_2O_T solubility in silicate melts have been developed allowing for the proportions of dissolved OH and H_2O_m to be calculated for a known concentration of H_2O_T (e.g., Silver and Stolper 1985; Silver et al. 1990). We calculate the OH contents of glasses in our experimental run products using the speciation model developed by Silver and Stolper (1985) and implemented in VolatileCalc (hereafter VolatileCalc) for basalt (49 wt. % SiO_2) at 1000 °C (Newman and Lowenstern 2002). We find that the relationship between olivine H_2O_T and glass OH concentrations is linear (i.e., $D_{OH}^{ol/melt}$ is constant; Fig. 9a), consistent with partitioning of OH between olivine and melt.

We calculate $D_{OH}^{ol/melt}$ from our measured olivine H_2O_T concentrations and calculated glass OH concentrations (Table 4) and find that it is invariant over the entire dataset ($D_{OH}^{ol/melt}$ = 0.0011±0.0002; 1 std. dev.), excluding San Carlos olivine seed grains. If we instead calculate $D_{OH}^{ol/melt}$only from H_2O-saturated experiments in which we are certain olivine grains were grown (B-09, B-10, G5, G7, M7, M8), we calculate a $D_{OH}^{ol/melt} = 0.0011 \pm 0.0001$ (1 std. dev.), which is indistinguishable from the value generated by the full dataset (0.0011±0.0002). We elect to adopt a $D_{OH}^{ol/melt}$ = 0.0011±0.0002 as generated from the full dataset due to the larger uncertainty. To evaluate whether the observed trend between $D_{H_2O_T}^{ol/melt}$ and melt H_2O_T concentration is related to the speciation of H in the melt, we need to convert our constant $D_{OH}^{ol/melt}$ to $D_{H_2O_T}^{ol/melt}$. We define our converted $D_{OH}^{ol/melt}$ as $\left(D_{H_2O_T}^{ol/melt}\right)_{conv}$, by 1) calculating the concentration of OH in the melt for a given concentration of H_2O_T using a H speciation model (in our case VolatileCalc), 2) taking our constant $D_{OH}^{ol/melt}$ (0.0011) and calculating the

This is the peer-reviewed, final accepted version for American Mineralogist, published by the Mineralogical Society of America.
The published version is subject to change. Cite as Authors (Year) Title. American Mineralogist, in press.
DOI: https://doi.org/10.2138/am-2025-9738. http://www.minsocam.org/

equilibrium concentration of H_2O_T in the olivine, and 3) calculate $\left(D_{H_2O_T}^{ol/melt}\right)_{conv}$ from the given melt and calculated olivine H_2O_T concentrations. We find that the curve for $\left(D_{H_2O_T}^{ol/melt}\right)_{conv}$ reproduces the relationship between $D_{H_2O_T}^{ol/melt}$ and glass H_2O_T concentration for our experiments (Fig. 9b). Altogether, this implies that the observed trend of decreasing $D_{H_2O_T}^{ol/melt}$ with increasing melt H_2O_T in our dataset is driven by variations in the melt H_2O_m content (i.e., the speciation of H in the melt). In simpler terms, the proportion of OH to H_2O_m in the melt exerts a primary control on the partitioning of H_2O_T between olivine and melt at the conditions of our experiments. We note that the speciation of H in the melt (e.g., OH, H_2O_m) is a function of $f H_2O$ in the melt.

Implications of a constant $D_{OH}^{ol/melt}$ on hydrogen incorporation in olivine

Considering that $D_{OH}^{ol/melt}$ is constant in our experiments and that the concentration of OH^- in the melt is proportional to $\sqrt{f_{H_2O}}$, it is therefore implied that the concentration of OH (assumed to be equivalent to H_2O_T) in olivine is proportional to $\sqrt{f_{H_2O}}$ as seen by:

$$D_{OH}^{Ol/melt} = d = \frac{C_{Ol}^{OH}}{C_{melt}^{OH}} \propto \frac{C_{Ol}^{OH}}{e\sqrt{f_{H_2O}}} \quad \Rightarrow \quad C_{Ol}^{OH} \propto de\sqrt{f_{H_2O}} \propto \sqrt{f_{H_2O}} \quad \#(4)$$

where C_{Ol}^{OH} and C_{melt}^{OH} are the concentration of OH in the olivine and melt, and d, and e are constants. A proportionality of C_{Ol}^{OH} ($[(OH)_O^*]$ in Kröger-Vink notation) to $\sqrt{f_{H_2O}}$ is most consistent with the charge neutrality conditions of $[(OH)_O^*] = \left[\left\{(OH)_O^* - V_{Me}^{//}\right\}^{/}\right]$ or $[(OH)_O^*] = 3\left[(H)_{Si}^{///}\right]$ (Table 1); although we acknowledge additional charge neutrality conditions not considered here may also reproduce this relationship. However, infrared measurements of natural olivine grains suggest H can occupy several different defects in a single olivine grain (e.g., Ferriss et al. 2018; Tollan et al. 2018; Barth et al. 2019). Therefore, it is likely that a suite of H-

This is the peer-reviewed, final accepted version for American Mineralogist, published by the Mineralogical Society of America.
The published version is subject to change. Cite as Authors (Year) Title. American Mineralogist, in press.
DOI: https://doi.org/10.2138/am-2025-9738. http://www.minsocam.org/

bearing defects exists in any given olivine grain such that the net proportionality of $[(OH)_O^*]$ to $f\mathrm{H_2O}$ is approximately $[(OH)_O^*] \propto \sqrt{f_{H_2O}}$. From this standpoint, it is also useful to consider a generalized notation that does not assign defect pairings to $(OH)_O^*$ in the olivine structure. We detail several equilibria describing H incorporation in olivine following the generalized notation of Keppler and Bolfan-Casanova (2006) in Supplement S1.2. In short, the condition of $C_{Ol}^{OH} \propto \sqrt{f_{H_2O}}$ is only satisfied through incorporation of H^+ as independent OH groups (e.g., OH is independent, whereas $(OH)_2$ is a cluster of 2 OH groups), as defined by:

$$H_2O_m^{melt} + O^{Ol} = 2OH^{Ol} \#(4)$$

in which molecular H_2O in a coexisting melt ($H_2O_m^{melt}$) reacts with an oxygen in the olivine lattice (O^{Ol}) to create two independent OH groups (OH^{Ol}).

IMPLICATIONS

Application to magma decompression rates

The relationship between $D_{H_2O_T}^{ol/melt}$ and melt H_2O_T content (or pressure if H_2O-saturated) is an important parameter for constraining magma decompression rates from H diffusion in olivine as it sets the equilibrium boundary condition between the olivine and the melt (Demouchy et al. 2006; Ferriss et al. 2018; Newcombe et al. 2020b). Prior studies have assumed a constant $D_{H_2O_T}^{ol/melt}$ value, which, to a first order, may be a reasonable assumption given that our experimental results are broadly consistent with the constant 500 – 2000 MPa $D_{H_2O_T}^{ol/melt}$ value from Towbin et al. (2023). However, our experimental results show that $D_{H_2O_T}^{ol/melt}$ varies over pressures relevant to magmas ascent, primarily as a function of H speciation in the melt and is only expected to vary strongly with pressure at H_2O-saturation. Allowing $D_{H_2O_T}^{ol/melt}$ to vary with

This is the peer-reviewed, final accepted version for American Mineralogist, published by the Mineralogical Society of America.
The published version is subject to change. Cite as Authors (Year) Title. American Mineralogist, in press.
DOI: https://doi.org/10.2138/am-2025-9738. http://www.minsocam.org/

melt H_2O_T or pressure may result in lower estimates for magma decompression rates than models with a constant $D_{H_2O_T}^{ol/melt}$ akin to Towbin et al. (2023). To assess the effect of a variable $D_{H_2O_T}^{ol/melt}$ on magma decompression rates, we apply the 1-D diffusion model of Newcombe et al. (2020b) to grain Seguam-Ol1 from Newcombe et al. (Fig. 10; 2020b). For each modelling run, we assume an initial pressure of 320 MPa, a constant temperature, a final pressure of 0.1 MPa (i.e., atmospheric pressure), and that the magma decompresses at a constant rate following a closed-system degassing curve (calculated using VolatileCalc; Newman and Lowenstern 2002) with an initial H_2O_T content of 4.2 wt. %. The associated code for the model of Newcombe et al. (2020b) performs a number of Monte Carlo simulations as a way to quantify uncertainty due to variation in model parameters. For each simulation, a synthetic H_2O_T concentration profile is generated by adding noise to the measured data points, and random starting values for the diffusivity of H in olivine (hereafter $Diff_H$) and decompression rate (hereafter dP/dt) are selected from normal distributions of log($Diff_H$) and log(dP/dt). The range of log($Diff_H$) values is calculated from the temperature-dependent parameterization of Barth et al. (2019) at temperatures from 1050 °C to 1090 °C (Newcombe et al. 2020b). In the original model, random values of $D_{H_2O_T}^{ol/melt}$ were selected from a uniform distribution across the range 0.0005 to 0.0009, but for the purposes of this comparison, we assume no uncertainty in the choice or parameterization of $D_{H_2O_T}^{ol/melt}$. For ease of adaptation of existing code, we parameterize $D_{H_2O_T}^{ol/melt}$ based upon the exponential fit to the relationship between olivine and melt H_2O_T concentrations for our experiments (Fig. 5c; $C_{H_2O_T}^{Ol} = 10.5198\left(C_{H_2O_T}^{melt}\right)^{0.5204}$; hereafter the "exponential relation"). While the exponential relation is not a direct calculation of $D_{H_2O_T}^{ol/melt}$, we note that it is a mathematical reconfiguration of $D_{H_2O_T}^{ol/melt}$ when the H_2O_T concentration of the melt is known. We also consider a constant

This is the peer-reviewed, final accepted version for American Mineralogist, published by the Mineralogical Society of America.
The published version is subject to change. Cite as Authors (Year) Title. American Mineralogist, in press.
DOI: https://doi.org/10.2138/am-2025-9738. http://www.minsocam.org/

678 $D_{H_2O_T}^{ol/melt}$ value of 0.00055, determined via measurement of olivine-melt inclusion pairs from the
679 1977 eruption of Seguam volcano. At the beginning of each simulation, an initial H_2O_T
680 concentration in the olivine crystal is calculated by multiplying $D_{H_2O_T}^{ol/melt}$ by the initial H_2O_T
681 concentration in the surrounding magma (4.2 wt. % H_2O_T). The H_2O_T concentration at the edge
682 of the olivine decreases throughout the simulation in response to constant decompression along a
683 closed-system degassing curve – at each decompression step, the H_2O_T concentration at the edge
684 of the olivine is calculated by multiplying the H_2O_T concentration of the melt by $D_{H_2O_T}^{ol/melt}$. In
685 response to the decreasing H_2O_T concentration at the edges of the olivine crystal, H diffuses from
686 the interior to the edge. This process continues until the magma reaches the final pressure in the
687 model, at which point the calculated H_2O_T gradient is compared to the measured gradient. For
688 each Monte Carlo simulation, the MATLAB function *fminsearch* is used to perform a global
689 minimization by varying dP/dt to achieve the best fit between the model and the synthetic data
690 (as assessed by the sum of the squared residuals). We find that the median magma
691 decompression rate (0.031 MPa/s) calculated using the exponential relation is ~2.5 times slower
692 than the median magma decompression rate calculated using a constant $D_{H_2O_T}^{ol/melt} = 0.00055$
693 (0.075 MPa/s). We note that the median decompression rate for the model using the exponential
694 relation (0.031 MPa/s) is within uncertainty of the model results from Newcombe et al. (2020b)
695 for Seguam-ol1 (0.039±0.017 MPa/s), who assume a constant $D_{H_2O_T}^{ol/melt}$ value from the range
696 0.0005 to 0.0009 and a final pressure of 2 MPa, but is offset to a slightly lower central value.

697 For decompression to 0.1 MPa as modeled here, we find that using the exponential
698 relation produces a better visual fit at the edges of Seguam-ol1 than the model with a constant
699 $D_{H_2O_T}^{ol/melt}$ value. The good fit of the model using the exponential relation allows for equilibrium

This is the peer-reviewed, final accepted version for American Mineralogist, published by the Mineralogical Society of America.
The published version is subject to change. Cite as Authors (Year) Title. American Mineralogist, in press.
DOI: https://doi.org/10.2138/am-2025-9738. http://www.minsocam.org/

degassing to 0.1 MPa, contrary to the assumptions of Newcombe et al. (2020b) who assumed a fragmentation and quench pressure of 2 MPa to fit the 1-D diffusion model to their data. The assumption of a ~2 MPa quench pressure at Seguam was chosen to provide a good visual fit to the data and because matrix glass compositions in Seguam pyroclasts (0.06 – 0.22 wt. H_2O_T; 15 – 40 μg/g CO_2; Newcombe et al. 2020b) are consistent with pressures of a few MPa. Notably, the diffusivity of H_2O_T in melt decreases with decreasing H_2O_T concentration (Ni and Zhang 2018) to values in melts containing < 0.5 wt. % H_2O_T that are approximately 2 orders of magnitude lower than the diffusivity of H in olivine at Seguam (Mutch et al. 2024). Therefore, it seems plausible that H diffusion in olivine may be a more sensitive recorder of the latest stages of decompression than melt embayments for systems that are degassing or have low total H contents. We note that the assumption of a constant dP/dt and the 1-D configuration in the model of Newcombe et al. (2020b) are likely oversimplifications and may alter the shapes of H_2O_T concentration gradients (Lloyd et al. 2014; Su and Huber 2017; Barth et al. 2019; Harris et al. 2024; Mutch et al. 2024). The model of Newcombe et al. (2020b) may be further improved by removing the assumptions of isothermal ascent (Newcombe et al. 2020a), closed-system equilibrium degassing of the melt, and a constant $D_{H_2O_T}^{ol/melt}$. Overall, our modelling results emphasize the need for careful choice of $D_{H_2O_T}^{ol/melt}$ when modelling magma decompression rates and that prior estimates for magma decompression rates based upon H^+ diffusion in olivine may be slightly overestimated. Furthermore, our results permit equilibrium degassing of olivine to atmospheric pressure, suggesting that H_2O_T concentration gradients in the outer several micrometers to few 10's of micrometers are sensitive to the final few MPa of decompression prior to quenching. Future work to constrain the relative sensitivity of H_2O_T gradients in the outer few micrometers in 3-D geometries and during non-linear decompression may provide

This is the peer-reviewed, final accepted version for American Mineralogist, published by the Mineralogical Society of America.
The published version is subject to change. Cite as Authors (Year) Title. American Mineralogist, in press.
DOI: https://doi.org/10.2138/am-2025-9738. http://www.minsocam.org/

723 further insights into the final few MPa of magma decompression. In the meantime, 1-D diffusion
724 modelling of core-edge H_2O_T gradients in olivine crystals remains a robust measure of mean
725 magma decompression rate across eruptions (for which dP/dt is known to vary by several orders
726 of magnitude), because uncertainties associated with $D_{H_2O_T}^{ol/melt}$ are relatively small (e.g., less than
727 an order of magnitude).

728 **Is H speciation in the melt a primary control on $D_{H_2O_T}^{min/melt}$ for NAMs?**

729 Prior work by Adam et al. (2016) showed that $D_{H_2O_T}^{cpx/melt}$ is partially dependent upon the
730 speciation of H in silicate melts. Adam et al. (2016) fit a constant $D_{OH}^{cpx/melt} = 0.5$ to the
731 relationship between $D_{H_2O_T}^{cpx/melt}$ and melt H_2O_T concentration, which visually fits the literature
732 dataset with scatter attributed to crystal compositional controls (i.e., clinopyroxene composition).
733 A similar result was found by Sarafian et al. (2019), who found a higher $D_{H_2O_T}^{cpx/melt}$ than
734 predicted by the clinopyroxene compositionally dependent model of O'Leary et al. (2010) for an
735 experiment at 0.1 MPa. Adam et al. (2016) also hypothesized that $D_{H_2O_T}^{min/melt}$ for orthopyroxene
736 and olivine are dependent upon the speciation of H in silicate melts. Similar to clinopyroxene,
737 we find here that $D_{H_2O_T}^{Ol/melt}$ is dependent upon the speciation of H in silicate melts, supporting the
738 hypothesis of Adam et al. (2016). For plagioclase, Hamada et al. (2013) found that plagioclase
739 and melt OH^- concentrations are proportional, consistent with a constant $D_{OH}^{Pl/melt}$ and with the
740 speciation of H in silicate melts controlling $D_{H_2O_T}^{Pl/melt}$, with a $D_{OH}^{Pl/melt} = 0.006$ (Castilla et al.
741 2024). Similarly, Xu et al. (2024) found a strong dependence of $D_{H_2O_T}^{Pl/melt}$ on melt H_2O_T
742 concentration which they suggest is likely due to variations in H-speciation and fH_2O. Overall, at
743 minimum for low H_2O_T systems, published experimental work on olivine (this study),

This is the peer-reviewed, final accepted version for American Mineralogist, published by the Mineralogical Society of America.
The published version is subject to change. Cite as Authors (Year) Title. American Mineralogist, in press.
DOI: https://doi.org/10.2138/am-2025-9738. http://www.minsocam.org/

clinopyroxene (Adam et al. 2016), and plagioclase (Hamada et al. 2013; Xu et al. 2024) is consistent with the speciation of H in silicate melts controlling $D_{H_2O_T}^{min/melt}$ for NAMs. Further experimental work on these phases, as well as orthopyroxene and garnet are necessary to evaluate whether partitioning of the speciation of H in silicate melts is a dominant control on $D_{H_2O_T}^{min/melt}$ for all NAMs.

Hygrometry applications

With careful application of $D_{H_2O_T}^{ol/melt}$, the H_2O_T concentration of olivine may also be used as a hygrometer for magmatic source regions in the Earth and other terrestrial bodies (e.g., the Moon, planetesimals), similar to pyroxene and plagioclase (e.g., Lin et al. 2019; Sarafian et al. 2019; Urann et al. 2022; Newcombe et al. 2023; Peterson et al. 2023, 2024; Stephant et al. 2023). A simple application of our results to natural systems would be to apply the relationship between olivine and melt H_2O_T concentrations (Fig. 5c) to measurements of H_2O_T in olivine, thereby calculating a melt H_2O_T concentration. However, applying the relation for olivine-melt H_2O_T concentrations as defined in our experiments requires the natural system to be under similar conditions (e.g., P, composition) to our experiments. A more generalized application of our results would be to take the constant $D_{OH}^{ol/melt}$ (0.0011±0.0002; 1 std. dev.), apply it to a measurement of OH^- in olivine to calculate melt OH^-, and then use a H-speciation model, such as the speciation model built into VolatileCalc (Newman and Lowenstern 2002), to determine the H_2O_T content of the melt. We urge some caution in applying the constant $D_{OH}^{ol/melt}$ to systems with highly disparate conditions to our experiments (e.g., high- or low- $aSiO_2$, olivine enriched in cations of particular charge such as Sc^{3+} or Ti^{4+}, pressures > ~1000 MPa) as significant deviations may result in the predominance and stabilization of different H-bearing defects in

766 olivine (e.g., Tollan et al. 2017; Fei and Katsura 2020), thereby altering the relationships
767 between $f\mathrm{H_2O}$, $C_{H_2O_T}^{ol}$, and $D_{OH}^{ol/melt}$. Experimental and methodological advancements are
768 necessary to reliably quench H_2O -saturated, glassy melts at pressures > ~500 MPa such that
769 H_2O_T solubility and speciation in silicate melts and ultimately mineral-melt H_2O_T partition
770 coefficients can be reliably determined.

771 **Summary and conclusions**

772 We have measured the H_2O_T concentrations of experimentally produced olivine and glass
773 at pressures ranging from 10 – 200 MPa. These data were used to provide the first constraints on
774 $D_{H_2O_T}^{ol/melt}$ at H_2O-saturated conditions and pressures below 500 MPa. We find that $D_{H_2O_T}^{ol/melt}$
775 decreases with pressure for the conditions of our experiments, contrary to extrapolations of a
776 constant (Towbin et al. 2023) or increasing (Novella et al. 2014; Adam et al. 2016) $D_{H_2O_T}^{ol/melt}$
777 value from high pressure experiments. The decrease of $D_{H_2O_T}^{ol/melt}$ with pressure from 10 – 200
778 MPa is reasonably explained by partitioning of OH between the olivine and melt. In turn, this
779 may imply that H speciation in the melt exerts an important control on the partitioning of H_2O_T
780 between NAMs and melt as inferred from experiments examining olivine, clinopyroxene, and
781 plagioclase. Our findings suggest that $D_{H_2O_T}^{min/melt}$ values for systems with low H_2O_T
782 concentrations (e.g., low pressure systems such as planetesimals or shallow magma reservoirs)
783 may be higher than previously expected and care needs to be taken in selecting $D_{H_2O_T}^{min/melt}$ for
784 modelling work. Overall, we suggest that the speciation of H in silicate melts exerts a primary
785 control on the partitioning of H_2O_T between olivine and melt.
786
787

Acknowledgements

We would like to thank Tim Grove for supplying an aliquot of powdered sample 82-72f from Medicine Lake, Volcano, CA USA as well as for providing experimental run products analyzed as part of this study. We would like to thank Dave Kohlstedt for conversations surrounding H incorporation mechanisms in olivine. We would also like to thank Terry Plank, Sarah Arden, and Louise Bolge for characterizing the bulk composition of the starting material from Mt. Pavlof used in this study. We thank Rick Hervig for a thorough, constructive review that helped to improve the manuscript. We acknowledge the support of the University of Maryland NanoCenter and the Advanced Imaging and Microscopy Lab (AIMLab). This work was supported by NASA FINESST [grant number 80NSSC22K0043] awarded to LDP. MEN and SGN acknowledge support from NASA Emerging Worlds [grant number 80NSSC20K0336]. MEN acknowledges support from NSF Petrology and Geochemistry [grant number 2017897]. GAG acknowledges support from NSF Marine Geology and Geophysics [grant number 2135901].

References

Adam, J., Turner, M., Hauri, E.H., and Turner, S. (2016) Crystal/melt partitioning of water and other volatiles during the near-solidus melting of mantle peridotite: Comparisons with non-volatile incompatible elements and implications for the generation of intraplate magmatism. American Mineralogist, 101, 876–888.

Alex, A., and Zajacz, Z. (2020) A new method to quantitatively control oxygen fugacity in externally heated pressure vessel experiments. European Journal of Mineralogy, 32, 219–234.

Aubaud, C., Hauri, E.H., and Hirschmann, M.M. (2004) Hydrogen partition coefficients between nominally anhydrous minerals and basaltic melts. Geophysical Research Letters, 31, 1–4.

Aubaud, C., Withers, A.C., Hirschmann, M.M., Guan, Y., Leshin, L.A., Mackwell, S.J., and Bell, D.R. (2007) Intercalibration of FTIR and SIMS for hydrogen measurements in glasses and nominally anhydrous minerals. American Mineralogist, 92, 811–828.

Bartels, K.S., Kinzler, R.J., and Grove, T.L. (1991) High pressure phase relations of primitive high-alumina basalts from Medicine Lake volcano, northern California. Contributions to Mineralogy and Petrology, 108, 253–270.

Barth, A., Newcombe, M., Plank, T., Gonnermann, H., Hajimirza, S., Soto, G.J., Saballos, A., and Hauri, E. (2019) Magma decompression rate correlates with explosivity at basaltic volcanoes — Constraints from water diffusion in olivine. Journal of Volcanology and Geothermal Research, 387, 106664.

Behrens, H. (2021) Hydrogen defects in feldspars: defect properties and implications for water solubility in feldspar. Physics and Chemistry of Minerals, 48, 8.

Berry, A.J., O'Neill, H.St.C., Hermann, J., and Scott, D.R. (2007) The infrared signature of water associated with trivalent cations in olivine. Earth and Planetary Science Letters, 261, 134–142.

Botcharnikov, R.E., Behrens, H., and Holtz, F. (2006) Solubility and speciation of C–O–H fluids in andesitic melt at T=1100–1300°C and P=200 and 500MPa. Chemical Geology, 229, 125–143.

Burnham, C.W., and Davis, N.F. (1974) The role of H_2O in silicate melts; II, Thermodynamic and phase relations in the system $NaAlSi_3O_8$-H_2O to 10 kilobars, 700-1100 °C. American Journal of Science, 274, 902–940.

Castilla, S.C., Newcombe, M.E., Piccoli, P.M., and Peterson, L.D. (2024) Crystals and Melt Inclusions Record Deep Storage of Superhydrous Magma Prior to the Largest Known Eruption of Cerro Machín Volcano, Colombia. Journal of Petrology, 65, egae095.

Costa, F., Shea, T., and Ubide, T. (2020) Diffusion chronometry and the timescales of magmatic processes. Nature Reviews Earth & Environment, 1, 201–214.

Crank, J. (1979) The Mathematics of Diffusion, 428 p. Clarendon Press.

Demouchy, S. (2021) Defects in olivine. European Journal of Mineralogy, 33, 249–282.

Demouchy, S., and Alard, O. (2021) Hydrogen, trace, and ultra-trace element distribution in natural olivines. Contributions to Mineralogy and Petrology, 176, 26.

Demouchy, S., Jacobsen, S.D., Gaillard, F., and Stern, C.R. (2006) Rapid magma ascent recorded by water diffusion profiles in mantle olivine. Geology, 34, 429–432.

Donnelly-Nolan, J.M., Champion, D.E., Grove, T.L., Baker, M.B., Taggart, J.E., and Bruggman, P.E. (1991) The Giant Crater Lava Field: Geology and geochemistry of a compositionally zoned, high-alumina basalt to basaltic andesite eruption at Medicine Lake Volcano, California. Journal of Geophysical Research: Solid Earth, 96, 21843–21863.

Fei, H., and Katsura, T. (2020) Pressure Dependence of Proton Incorporation and Water Solubility in Olivine. Journal of Geophysical Research: Solid Earth, 125, e2019JB018813.

Ferriss, E., Plank, T., Newcombe, M., Walker, D., and Hauri, E. (2018) Rates of dehydration of olivines from San Carlos and Kilauea Iki. Geochimica et Cosmochimica Acta, 242, 165–190.

Gaetani, G.A., Grove, T.L., and Bryan, W.B. (1994) Experimental phase relations of basaltic andesite from hole 839B under hydrous and anhydrous conditions. Proceedings of the Ocean Drilling Program, scientific results, 135.

Gale, A., Dalton, C.A., Langmuir, C.H., Su, Y., and Schilling, J.-G. (2013) The mean composition of ocean ridge basalts. Geochemistry, Geophysics, Geosystems, 14, 489–518.

Grant, K.J., Kohn, S.C., and Brooker, R.A. (2007) The partitioning of water between olivine, orthopyroxene and melt synthesised in the system albite–forsterite–H_2O. Earth and Planetary Science Letters, 260, 227–241.

Hall, L.J., Brodie, J., Wood, B.J., and Carroll, M.R. (2004) Iron and water losses from hydrous basalts contained in Au80Pd20 capsules at high pressure and temperature. Mineralogical Magazine, 68, 75–81.

Hamada, M., Ushioda, M., Fujii, T., and Takahashi, E. (2013) Hydrogen concentration in plagioclase as a hygrometer of arc basaltic melts: Approaches from melt inclusion analyses and hydrous melting experiments. Earth and Planetary Science Letters, 365, 253–262.

Harris, M., Hosseini, B., Myers, M., and Bouley, L. (2024) Reconciling petrologic magma ascent speedometers for the June 12th, 1991 eruption of Mt. Pinatubo, Philippines. Volcanica, 7, 117–133.

Hauri, E., Wang, J., Dixon, J.E., King, P.L., Mandeville, C., and Newman, S. (2002) SIMS analysis of volatiles in silicate glasses 1. Calibration, matrix effects and comparisons with FTIR. Chemical Geology, 16.

Hauri, E.H., Shaw, A.M., Wang, J., Dixon, J.E., King, P.L., and Mandeville, C. (2006a) Matrix effects in hydrogen isotope analysis of silicate glasses by SIMS. Chemical Geology, 235, 352–365.

Hauri, E.H., Gaetani, G.A., and Green, T.H. (2006b) Partitioning of water during melting of the Earth's upper mantle at H_2O-undersaturated conditions. Earth and Planetary Science Letters, 248, 715–734.

Iacovino, K., Matthews, S., Wieser, P.E., Moore, G.M., and Bégué, F. (2021) VESIcal Part I: An Open-Source Thermodynamic Model Engine for Mixed Volatile (H_2O-CO_2) Solubility in Silicate Melts. Earth and Space Science, 8, e2020EA001584.

Jollands, M.C., Kempf, E., Hermann, J., and Müntener, O. (2019) Coupled inter-site reaction and diffusion: Rapid dehydrogenation of silicon vacancies in natural olivine. Geochimica et Cosmochimica Acta, 262, 220–242.

Keppler, H., and Bolfan-Casanova, N. (2006) Thermodynamics of Water Solubility and Partitioning. Reviews in Mineralogy and Geochemistry, 62, 193–230.

Koga, K., Hauri, E., Hirschmann, M., and Bell, D. (2003) Hydrogen concentration analyses using SIMS and FTIR: Comparison and calibration for nominally anhydrous minerals: hydrogen concentration analyses. Geochemistry, Geophysics, Geosystems, 4, 1–20.

Kohlstedt, D.L., and Mackwell, S.J. (1998) Diffusion of Hydrogen and Intrinsic Point Defects in Olivine. Zeitschrift für Physikalische Chemie, 207, 147–162.

Kovalenko, V.I., Naumov, V.B., Girnis, A.V., Dorofeeva, V.A., and Yarmolyuk, V.V. (2010) Average composition of basic magmas and mantle sources of island arcs and active continental margins estimated from the data on melt inclusions and quenched glasses of rocks. Petrology, 18, 1–26.

Kumamoto, K.M., Warren, J.M., and Hauri, E.H. (2017) New SIMS reference materials for measuring water in upper mantle minerals. American Mineralogist, 102, 537–547.

900 Li, Z.-X.A., Lee, C.-T.A., Peslier, A.H., Lenardic, A., and Mackwell, S.J. (2008) Water contents
901 in mantle xenoliths from the Colorado Plateau and vicinity: Implications for the mantle
902 rheology and hydration-induced thinning of continental lithosphere. Journal of
903 Geophysical Research: Solid Earth, 113.

904 Lin, Y.H., Hui, H., Li, Y., Xu, Y., and van Westrenen, W. (2019) A lunar hygrometer based on
905 plagioclase-melt partitioning of water. Geochemical Perspectives Letters, 10, 14–19.

906 Lloyd, A.S., Ruprecht, P., Hauri, E.H., Rose, W., Gonnermann, H.M., and Plank, T. (2014)
907 NanoSIMS results from olivine-hosted melt embayments: Magma ascent rate during
908 explosive basaltic eruptions. Journal of Volcanology and Geothermal Research, 283, 1–
909 18.

910 Médard, E., and Grove, T.L. (2008) The effect of H_2O on the olivine liquidus of basaltic melts:
911 experiments and thermodynamic models. Contributions to Mineralogy and Petrology,
912 155, 417–432.

913 Mitchell, A.L., Gaetani, G.A., O'Leary, J.A., and Hauri, E.H. (2017) H_2O solubility in basalt at
914 upper mantle conditions. Contributions to Mineralogy and Petrology, 172, 85.

915 Moore, G., Vennemann, T., and Carmichael, I.S.E. (1998) An empirical model for the solubility
916 of H_2O in magmas to 3 kilobars. American Mineralogist, 83, 36–42.

917 Mosenfelder, J.L., and Rossman, G.R. (2013) Analysis of hydrogen and fluorine in pyroxenes: I.
918 Orthopyroxene. American Mineralogist, 98, 1026–1041.

Moussallam, Y., Towbin, W.H., Plank, T., Bureau, H., Khodja, H., Guan, Y., Ma, C., Baker, M.B., Stolper, E.M., Naab, F.U., and others (2024) ND70 Series Basaltic Glass Reference Materials for Volatile Element (HO, CO, S, Cl, F) Measurement and the C Ionisation Efficiency Suppression Effect of Water in Silicate Glasses in SIMS. Geostandards and Geoanalytical Research, 48, 637–660.

Mutch, E.J.F., Newcombe, M.E., and Rudge, J.F. (2024) 3D Diffusion of Water in Melt Inclusion-Bearing Olivine Phenocrysts. Geochemistry, Geophysics, Geosystems, 25, e2023GC011365.

Newcombe M. E. (2022) SIMSblank. v2.0 (Version 2.0). Zenodo. doi.org/10.5281/zenodo.7220990.

Newcombe, M.E., Brett, A., Beckett, J.R., Baker, M.B., Newman, S., Guan, Y., Eiler, J.M., and Stolper, E.M. (2017) Solubility of water in lunar basalt at low pH_2O. Geochimica et Cosmochimica Acta, 200, 330–352.

Newcombe, M.E., Plank, T., Zhang, Y., Holycross, M., Barth, A., Lloyd, A.S., Ferguson, D., Houghton, B.F., and Hauri, E. (2020a) Magma Pressure-Temperature-Time Paths During Mafic Explosive Eruptions. Frontiers in Earth Science, 8.

Newcombe, M.E., Plank, T., Barth, A., Asimow, P.D., and Hauri, E. (2020b) Water-in-olivine magma ascent chronometry: Every crystal is a clock. Journal of Volcanology and Geothermal Research, 398, 106872.

Newcombe, M.E., Nielsen, S.G., Peterson, L.D., Wang, J., Alexander, C.M.O'D., Sarafian, A.R., Shimizu, K., Nittler, L.R., and Irving, A.J. (2023) Degassing of early-formed planetesimals restricted water delivery to Earth. Nature, 615, 854–857.

Newman, S., and Lowenstern, J.B. (2002) VolatileCalc: a silicate melt–H_2O–CO_2 solution model written in Visual Basic for excel. Computers & Geosciences, 28, 597–604.

Newman, S., Epstein, S., and Stolper, E. (1988) Water, carbon dioxide, and hydrogen isotopes in glasses from the ca. 1340 A.D. eruption of the Mono Craters, California: Constraints on degassing phenomena and initial volatile content. Journal of Volcanology and Geothermal Research, 35, 75–96.

Ni, H., and Zhang, L. (2018) A general model of water diffusivity in calc-alkaline silicate melts and glasses. Chemical Geology, 478, 60–68.

Novella, D., Frost, D.J., Hauri, E.H., Bureau, H., Raepsaet, C., and Roberge, M. (2014) The distribution of H_2O between silicate melt and nominally anhydrous peridotite and the onset of hydrous melting in the deep upper mantle. Earth and Planetary Science Letters, 400, 1–13.

O'Leary, J.A., Gaetani, G.A., and Hauri, E.H. (2010) The effect of tetrahedral Al^{3+} on the partitioning of water between clinopyroxene and silicate melt. Earth and Planetary Science Letters, 297, 111–120.

Peslier, A.H., and Luhr, J.F. (2006) Hydrogen loss from olivines in mantle xenoliths from Simcoe (USA) and Mexico: Mafic alkalic magma ascent rates and water budget of the sub-continental lithosphere. Earth and Planetary Science Letters, 242, 302–319.

Peterson, L.D., Newcombe, M.E., Alexander, C.M.O'D., Wang, J., Klein, F., Bekaert, D.V., and Nielsen, S.G. (2023a) The H content of aubrites: An evaluation of bulk versus in situ methods for quantifying water in meteorites. Earth and Planetary Science Letters, 620, 118341.

Peterson, L.D., Newcombe, M.E., Alexander, C.M.O'D., Wang, J., Sarafian, A.R., Bischoff, A., and Nielsen, S.G. (2023b) The H_2O content of the ureilite parent body. Geochimica et Cosmochimica Acta, 340, 141–157.

Peterson, L.D., Newcombe, M.E., Alexander, C.M.O'D., Wang, J., and Nielsen, S.G. (2024) The H-poor nature of incompletely melted planetesimals: The view from acapulcoites and lodranites. Geochimica et Cosmochimica Acta, 370, 1–14.

Pineau, F., Shilobreeva, S., Kadik, A., and Javoy, M. (1998) Water solubility and D/H fractionation in the system basaltic andesite–H_2O at 1250°C and between 0.5 and 3 kbars. Chemical Geology, 147, 173–184.

Pitzer, K.S., and Sterner, S.M. (1994) Equations of state valid continuously from zero to extreme pressures for H_2O and CO_2. The Journal of Chemical Physics, 101, 3111–3116.

Rasmussen, D., and Plank, T. (2021) Bulk rock data for the central-eastern Aleutian volcanoes. Interdisciplinary Earth Data Alliance (IEDA).

Russell, L. (1957) Solubility of water in molten glass. J Soc Glass Technol, 41, 3111–3116.

977 Sarafian, A.R., Nielsen, S.G., Marschall, H.R., Gaetani, G.A., Hauri, E.H., Righter, K., and
978 Sarafian, E. (2017) Angrite meteorites record the onset and flux of water to the inner
979 solar system. Geochimica et Cosmochimica Acta, 212, 156–166.

980 Sarafian, A.R., Nielsen, S.G., Marschall, H.R., Gaetani, G.A., Righter, K., and Berger, E.L.
981 (2019) The water and fluorine content of 4 Vesta. Geochimica et Cosmochimica Acta,
982 266, 568–581.

983 Sarafian, E., Gaetani, G.A., Hauri, E.H., and Sarafian, A.R. (2017) Experimental constraints on
984 the damp peridotite solidus and oceanic mantle potential temperature. Science, 355, 942–
985 945.

986 Schmidt, M.W., and Jagoutz, O. (2017) The global systematics of primitive arc melts.
987 Geochemistry, Geophysics, Geosystems, 18, 2817–2854.

988 Shimizu, K., Alexander, C.M.O'D., Hauri, E.H., Sarafian, A.R., Nittler, L.R., Wang, J.,
989 Jacobsen, S.D., and Mendybaev, R.A. (2021) Highly volatile element (H, C, F, Cl, S)
990 abundances and H isotopic compositions in chondrules from carbonaceous and ordinary
991 chondrites. Geochimica et Cosmochimica Acta, 301, 230–258.

992 Shimizu, K., Ushikubo, T., Kuritani, T., Hirano, N., and Yamashita, S. (2022) Modification for
993 the matrix effect in SIMS-derived water contents of silicate glasses. Geochemical
994 Journal, 56, 223–230.

995 Silver, L., and Stolper, E. (1985) A Thermodynamic Model for Hydrous Silicate Melts. The
996 Journal of Geology, 93, 161–177.

997 ——— (1989) Water in Albitic Glasses. Journal of Petrology, 30, 667–709.

998 Silver, L.A., Ihinger, P.D., and Stolper, E. (1990) The influence of bulk composition on the
999 speciation of water in silicate glasses. Contributions to Mineralogy and Petrology, 104,
1000 142–162.

1001 Stephant, A., Zhao, X., Anand, M., Davidson, J., Carli, C., Cuppone, T., Pratesi, G., and Franchi,
1002 I.A. (2023) Hydrogen in acapulcoites and lodranites: A unique source of water for
1003 planetesimals in the inner Solar System. Earth and Planetary Science Letters, 615,
1004 118202.

1005 Stolper, E. (1982a) The speciation of water in silicate melts. Geochimica et Cosmochimica Acta,
1006 46, 2609–2620.

1007 ——— (1982b) Water in silicate glasses: An infrared spectroscopic study. Contributions to
1008 Mineralogy and Petrology, 81, 1–17.

1009 Su, Y., and Huber, C. (2017) The effect of nonlinear decompression history on H_2O/CO_2
1010 vesiculation in rhyolitic magmas. Journal of Geophysical Research: Solid Earth, 122,
1011 2712–2723.

1012 Tenner, T.J., Hirschmann, M.M., Withers, A.C., and Hervig, R.L. (2009) Hydrogen partitioning
1013 between nominally anhydrous upper mantle minerals and melt between 3 and 5 GPa and
1014 applications to hydrous peridotite partial melting. Chemical Geology, 262, 42–56.

Tenner, T.J., Hirschmann, M.M., Withers, A.C., and Ardia, P. (2012) H_2O storage capacity of olivine and low-Ca pyroxene from 10 to 13 GPa: consequences for dehydration melting above the transition zone. Contributions to Mineralogy and Petrology, 163, 297–316.

Tollan, P.M.E., Smith, R., O'Neill, H.St.C., and Hermann, J. (2017) The responses of the four main substitution mechanisms of H in olivine to H_2O activity at 1050 °C and 3 GPa. Progress in Earth and Planetary Science, 4, 14.

Tollan, P.M.E., O'Neill, H.St.C., and Hermann, J. (2018) The role of trace elements in controlling H incorporation in San Carlos olivine. Contributions to Mineralogy and Petrology, 173, 89.

Tomlinson, J. (1956) A note on the solubility of water in a molten sodium silicate. J Soc Glass Technol, 40, 25–31.

Towbin, H., Plank, T., Klein, E., and Hauri, E.H. (2023) Measuring H_2O Concentrations in Olivine by Secondary Ion Mass Spectrometry: Challenges and Paths Forward. American Mineralogist, 108, 982–940.

Urann, B.M., Le Roux, V., Jagoutz, O., Müntener, O., Behn, M.D., and Chin, E.J. (2022) High water content of arc magmas recorded in cumulates from subduction zone lower crust. Nature Geoscience, 15, 501–508.

Weis, F.A., Skogby, H., Troll, V.R., Deegan, F.M., and Dahren, B. (2015) Magmatic water contents determined through clinopyroxene: Examples from the Western Canary Islands, Spain. Geochemistry, Geophysics, Geosystems, 16, 2127–2146.

1035 Workman, R.K., and Hart, S.R. (2005) Major and trace element composition of the depleted
1036 MORB mantle (DMM). Earth and Planetary Science Letters, 231, 53–72.

1037 Xu, Y., Lin, Y., Zheng, H., and van Westrenen, W. (2024) Non-Henrian behavior of hydrogen in
1038 plagioclase – Basaltic melt partitioning. Chemical Geology, 122153.

1039 Yang, Y., Liu, W., Qi, Z., Wang, Z., Smyth, J.R., and Xia, Q. (2019) Re-configuration and
1040 interaction of hydrogen sites in olivine at high temperature and high pressure. American
1041 Mineralogist, 104, 878–889.

1042 Zhang, M., Salje, E.K.H., Carpenter, M.A., Wang, J.Y., Groat, L.A., Lager, G.A., Wang, L.,
1043 Beran, A., and Bismayer, U. (2007) Temperature dependence of IR absorption of
1044 hydrous/hydroxyl species in minerals and synthetic materials. American Mineralogist, 92,
1045 1502–1517.

1046 Zhao, Y.-H., Ginsberg, S.B., and Kohlstedt, D.L. (2004) Solubility of hydrogen in olivine:
1047 dependence on temperature and iron content. Contributions to Mineralogy and Petrology,
1048 147, 155–161.

1049 Zimmer, M.M., Plank, T., Hauri, E.H., Yogodzinski, G.M., Stelling, P., Larsen, J., Singer, B.,
1050 Jicha, B., Mandeville, C., and Nye, C.J. (2010) The Role of Water in Generating the
1051 Calc-alkaline Trend: New Volatile Data for Aleutian Magmas and a New Tholeiitic
1052 Index. Journal of Petrology, 51, 2411–2444.

1053

1054

List of Figure Captions:

Fig. 1 Schematic diagrams showing the capsule set-up used in this study. A) Capsule set-up used for charges XP-02 to XP-05. B) Capsule set-up for all other charges. Capsule components are not to scale.

Fig. 2 Representative reflected light images of A) run products containing the Mt. Pavlof starting material (MPS) and B) run products containing natural basaltic starting material (BS) 82-72f from Medicine Lake Volcano. Ol – olivine, Plag – plagioclase. Images were collected without a blue-light filter resulting in a blue tone for all images.

Fig. 3 A) Olivine H_2O concentration, B) glass H_2O concentration, and C) $D_{H_2O_T}^{ol/melt}$ plotted against time for 100 MPa time series experiments. Filled symbols represent charges that were visually confirmed to be H_2O-saturated and were fully equilibrated (see **H Solubility in Olivine**). Open symbols represent data from experiments where H_2O saturation was not visually confirmed or may preserve a "seed effect" (see **Extrinsic point defects**).

Fig. 4 Olivine H_2O concentrations from MP run products (blue) and the H_2O concentration of seed olivine from the MPS starting material (grey box). Legend as in Fig. 3.

Fig. 5 Olivine H_2O_T concentrations plotted against A) pressure, B) fH_2O, C) glass H_2O_T, and D) olivine forsterite content (Fo) for newly conducted and newly analyzed prior experiments in this study. Dashed lines are least squares power law fits to data from charges that were visually confirmed to be H_2O-saturated and fully equilibrated (see **H Solubility in Olivine;** filled symbols) based upon the presence of liquid water or water vapor when capsules were opened. Open symbols represent data from experiments where H_2O saturation was not visually confirmed or may preserve a "seed effect" (see **Extrinsic point defects**). 82-72f is the basaltic starting

material from Medicine Lake Volcano, CA used in this study. We calculate fH_2O at H_2O saturation using the equation of state of Pitzer and Sterner (1994) as implemented in the calculator by Tony Withers (https://publish.uwo.ca/~awither5/fugacity/index.htm).

Fig. 6 Glass H_2O_T concentrations plotted against A) pressure and B) fH_2O for all newly conducted and newly analyzed prior experiments and C) for $Na_2O + K_2O$ for MP run products from experiments at 100 MPa. Dashed lines are least squares fits to the data with the exception of the empirical fit for glass H_2O_T to pressure from Botcharnikov et al. (2006). fH_2O calculated as in Fig. 5. Legend as in Fig. 5.

Fig. 7 $D_{H_2O_T}^{ol/melt}$ plotted against A) pressure, B) fH_2O, and C) the concentration of H_2O_T in the glass for all newly conducted and newly analyzed prior experiments in this study. Black dashed lines are empirical fits of a linear exponential loss function (see "**Results**") to all data, excluding San Carlos olivine. The grey field in panel A represents the 0.5 – 3 GPa $D_{H_2O_T}^{ol/melt}$ value from Towbin et al. (2023). The dotted red line in panel A represents a linear regression through the $D_{H_2O_T}^{ol/melt}$ data from Adam et al. (2016), Tenner et al. (2009), Tenner et al. (2012), Aubaud et al. (2004), Koga et al. (2003), Grant et al. (2007), Novella et al. (2014), and Hauri et al. (2006b) with revised values from Towbin et al. (2023) when available. fH_2O calculated as in Fig. 5. Legend as in Fig. 5.

Fig. 8 Comparison of the measured H_2O concentrations of San Carlos (SC) seed olivine and grown olivine from charges containing the basaltic (82-72f) starting material.

Fig. 9 a) Olivine H_2O_T concentration plotted against glass OH concentration, and b) $D_{H_2O_T}^{ol/melt}$ plotted against glass H_2O_T concentration. The dashed line in b) is a conversion of a constant

$D_{OH}^{ol/melt}$ (0.0011±0.0002) to $D_{H_2O_T}^{ol/melt}$. Please see text for description of how $\left(D_{H_2O_T}^{ol/melt}\right)_{conv.}$ is calculated. Legend as in Fig. 5.

Fig. 10 a) Modeled fit to the measured H_2O_T diffusion profile for Seguam-ol1 (black circles) from Newcombe et al. (2020b) using a constant $D_{H_2O_T}^{ol/melt} = 0.00055$ (red) and the exponential relation (Fig. 5c; see text; blue). Horizontal dashed lines correspond to the initial olivine H_2O_T calculated in the model. Note that the final pressure for both models is set to atmospheric pressure (0.1 MPa), which is different than the 2 MPa final pressure from Newcombe et al. (2020b). b) The diffusivity of H (D_H; values drawn from a log uniform distribution; see text) plotted against the best-fit magma decompression rate (dP/dt) for 25 iterations of the 1-D Monte Carlo model of Newcombe et al. (2020b) using a constant $D_{H_2O_T}^{ol/melt} = 0.00055$ (red) and the exponential relation (Fig. 5c; see text; blue). Scatter in panels A and B are predominantly due to uncertainty in the diffusivity of H in olivine ($logD_H$) and uncertainties in H_2O_T concentrations (assumed to be normally distributed with a standard deviation of ~1 µg/g H_2O_T based upon replicate analyses of secondary standard Herasil glass; see Newcombe et al. 2020b). Note that each model run is fit to a synthetic H_2O_T concentration profile created by adding noise to the original data. However, to aid in the comparison of the model results, only the original data (black circles) is plotted in panel a.

This is the peer-reviewed, final accepted version for American Mineralogist, published by the Mineralogical Society of America.
The published version is subject to change. Cite as Authors (Year) Title. American Mineralogist, in press.
DOI: https://doi.org/10.2138/am-2025-9738. http://www.minsocam.org/

Revision 1

Table 1) Dependence of hydrous defect concentrations on fH_2O under various charge neutrality conditions as the *exponent* r in the relation $[defect] \propto {f_{H_2O}}^r$ modified from Fei and Katsura (2020)

Charge Neutrality Condition	$[(OH)_O^*]$	$[H'_{Me}]$	$[(2H)_{Me}^X]$	$[H'''_{Si}]$	$[(2H)''_{Si}]$	$[(3H)'_{Si}]$	$[(4H)_{Si}^X]$
$[(OH)_O^*] = 4[(V)''''_{Si}]$	**2/5**	3/5	1	4/5	6/5	8/5	2
$[(OH)_O^*] = 3[(H)'''_{Si}]$	**1/2**	1/2	1	**1/2**	1	3/2	2
$[(OH)_O^*] = [2(2H)''_{Si}]$	**2/3**	1/3	1	0	**2/3**	4/3	2
$[(OH)_O^*] = [(3H)'_{Si}]$	**1**	0	1	-1	0	**1**	2
$[(OH)_O^*] = 2[V''_{Me}]$	**1/3**	2/3	1	1	4/3	5/3	2
$[Fe_{Me}^*] = [\{(OH)_O^* - V''_{Me}\}']$	**3/4**	**1/4**	1	-1/4	1/2	5/4	2
$[(OH)_O^*] = [\{(OH)_O^* - V''_{Me}\}']$	**1/2**	1/2	1	1/2	1	3/2	2

Bold – defect included in charge neutrality condition

[ ] – concentration, { } – grouped defects, * – positive charge relative to the typical charge of the site, ′ – negative charge relative to the typical charge of the site, × – neutral charge relative to the typical charge of the site Me – metal cation

1116

Revision 1

Table 2) Summary of Experimental Run Conditions

	Starting Materials	P (MPa)	T (°C)	Time (hr.)	fO_2 buffer	Measured fO_2 (log)	Unc.	ΔNNO	Evidence of Saturation
New Experiments									
XP-02	MP	99	1000	23:05	NNO	-9.5	0.1	0.7	Same weight; vesicular
XP-03	MP	85	1000	20:35	NNO	-9.3	0.2	0.9	H_2O visually confirmed
XP-05	MP	99	1000	25:30	NNO	-8.9	0.2	1.2	Vesicular
XP-06	MP	99	1000	12:15	NNO	-9.74	0.04	0.45	H_2O visually confirmed
XP-07	MP	30	1000	24:00	NNO				Vesicular
XP-09	MP & 82-72f*	99	1000	23:45	NNO				H_2O visually confirmed
XP-10	MP & 82-72f*	100	1000	24:00	NNO	-8.5	0.2	1.6	H_2O visually confirmed
XP-13	MP & 82-72f*	96	1000	48:00	NNO	-8.2	0.2	2.0	Same weight; vesicular

XP-14	MP	57	1000	24:00	NNO	-9.51	0.09	0.67	Vesicular
XP-15	MP	50	1000	24:00	NNO	-9.70	0.08	0.49	Capsule "popped" when opening; vesicular
XP-17	MP	52	1000	24:00	NNO				Vesicular
XP-18	MP	52	1000	24:00	NNO				Vesicular
XP-19	MP	53	1000	24:00	NNO				Vesicular

MP – basaltic-andesite starting material from Mt. Pavlof, AK; 82-72f – high-alumina basalt starting material from Medicine Lake Volcano, CA; *Note: Experiments XP-09, XP-10, and XP-13 contained two inner capsules, one with each starting material

This is the peer-reviewed, final accepted version for American Mineralogist, published by the Mineralogical Society of America.
The published version is subject to change. Cite as Authors (Year) Title. American Mineralogist, in press.
DOI: https://doi.org/10.2138/am-2025-9738. http://www.minsocam.org/

Revision 1

Table 2) Summary of Experimental Run Conditions (continued…)

	Starting Materials	P (MPa)	T (°C)	Time (h.r)	fO_2 buffer	Measured fO_2 (log)	Unc.	ΔNNO	Evidence of Saturation
Gaetani et al. (1994)									
G5	ODP B.A.	200	1020	24	NNO				H_2O visually confirmed
G7	ODP B.A.	200	1035	24	NNO				H_2O visually confirmed
Gaetani et al. (1994)									
M7	82-72f	100	1173	2	NNO				H_2O visually confirmed
M8	82-72f	50	1190	3.1	NNO				H_2O visually confirmed
M11	82-72f	25	1204	2	NNO				
M23	82-72f	10	1220	1.5	NNO				

MP - Mt. Pavlof basaltic andesitic ash; ODP B. A. - Ocean Drilling Program Sample 135-839B-15R-2, 63-67 cm

1120

1121

1122

Table 3) Composition of Proposed Starting Materials

Oxide (wt%)	Mt. Pavlof, 2016, Ash	82-72f	Lherzolite Melt[1]	N-MORB[2]	N-MORB[3]
SiO_2	54.2	47.7	50.0	49.51	50.42
TiO_2	1.12	0.59	0.73	0.9	1.53
Al_2O_3	17.9	18.5	17.6	16.75	15.13
FeO*	8.69	8.21	7.34	8.05	9.81
MnO	0.18	0.15	0.26	0.14	0.171
MgO	4.4	10.5	9.9	9.74	7.76
CaO	8.88	12	11.3	12.5	11.35
Na_2O	3.39	2.16	2.55	2.18	2.83
K_2O	0.66	0.07	0.16	0.07	0.14
P_2O_5	0.62	0.06	0.16	0.1	0.164

FeO* is all Fe reported as FeO

[1]Bartels et al. (1991)

[2]Workman and Hart (2005)

[3]Gale et al. (2013)

1124

1125

1126

This is the peer-reviewed, final accepted version for American Mineralogist, published by the Mineralogical Society of America.
The published version is subject to change. Cite as Authors (Year) Title. American Mineralogist, in press.
DOI: https://doi.org/10.2138/am-2025-9738. http://www.minsocam.org/

Revision 1

1127

Table 4) Summary of the H_2O_T contents of run products and predicted glass H_2O_T from the models of Moore et al. and VolatileCalc

		SIMS				Moore et al. (1998)	Calculated OH and H_2Om			
	Phase	H_2O_T (µg/g)	Unc.[1]	$D_{H_2O_T}^{ol/melt}$	Unc.	H_2O_T (µg/g)	OH	H_2Om	$D_{OH}^{ol/melt}$	Unc
MP-10	Glass	46500	4700	-	-	34635	1.92	2.73	-	-
	Olivine	20	3	0.00044	0.00007	-	-	-	0.0011	0.0002
MP-02	Glass	39900	3900	-	-	34620	1.85	2.14	-	-
	Olivine	17	2	0.00043	0.00006	-	-	-	0.0009	0.0001
MP-06	Glass	47600	4800	-	-	34365	1.93	2.83	-	-
	Olivine	16	2	0.00033	0.00005	-	-	-	0.00082	0.0001
MP-09	Glass	44200	4400	-	-	34060	1.90	2.52	-	-
	Olivine	24	2	0.00055	0.00006	-	-	-	0.00129	0.0002
MP-05	Glass	*34000*	*3400*	-	-	35060	1.76	1.64	-	-
	Olivine	*27*	*3*	0.0008	0.0001	-	-	-	0.0016	0.0002
MP-13	Glass	26000	2600	-	-	34669	1.57	1.03	-	-
	Olivine	20	2	0.0008	0.0001	-	-	-	0.0012	0.0002

This is the peer-reviewed, final accepted version for American Mineralogist, published by the Mineralogical Society of America.
The published version is subject to change. Cite as Authors (Year) Title. American Mineralogist, in press.
DOI: https://doi.org/10.2138/am-2025-9738. http://www.minsocam.org/

MP-03	Glass	41400	4100	-	-	31880	1.87	2.27	-	-
	Olivine	16	3	0.00040	0.00008	-	-	-	0.0009	0.0002
MP-14	Glass	24000	2400	-	-	25849	1.51	0.89	-	-
	Olivine	15	3	0.0006	0.0001	-	-	-	0.0010	0.0002
MP-19	Glass	16500	1700	-	-	25242	1.22	0.43	-	-
	Olivine	16	2	0.0009	0.0002	-	-	-	0.0013	0.0002
MP-17	Glass	13900	1400	-	-	24994	1.08	0.31	-	-
	Olivine	11	2	0.0008	0.0002	-	-	-	0.0011	0.0002
MP-18	Glass	14600	1500	-	-	24777	1.12	0.34	-	-
	Olivine	16	3	0.0011	0.0002	-	-	-	0.0014	0.0003
MP-15	Glass	15600	1600	-	-	24030	1.17	0.39	-	-
	Olivine	7	1	0.00044	0.00006	-	-	-	0.0006	0.0001

Table 4) Summary of the H_2O_T contents of run products and predicted glass H_2O_T from the models of Moore et al. and VolatileCalc

(continued…)

							Calculated			
						Moore et al.	OH and			
		SIMS				(1998)	H_2O_m			

This is the peer-reviewed, final accepted version for American Mineralogist, published by the Mineralogical Society of America.
The published version is subject to change. Cite as Authors (Year) Title. American Mineralogist, in press.
DOI: https://doi.org/10.2138/am-2025-9738. http://www.minsocam.org/

Revision 1

	Phase	H_2O_T (µg/g)	Unc.[1]	$D_{H_2O_T}^{ol/melt}$	Unc.	H_2O_T (µg/g)	OH	H_2Om	$D_{OH}^{ol/melt}$	Phase
MP-07	Glass	14800	1500	-	-	18117	1.13	0.35	-	-
	Olivine	16	1	0.0011	0.0001	-	-	-	0.0014	0.0002
B-09	Glass	27900	6100	-	-	34642	1.62	1.17	-	-
	Olivine	17	1	0.00062	0.00014	-	-	-	0.00106	0.0001
B-10	Glass	34100	6200	-	-	34829	1.76	1.65	-	-
	Olivine	20	4	0.0006	0.0001	-	-	-	0.0011	0.0002
	San Carlos	5.4	0.5	0.00016	0.00003				0.00031	0.00004
B-13	Glass	38600	4900	-	-	34077	1.83	2.03	-	-
	Olivine	23	7	0.0006	0.0002	-	-	-	0.0013	0.0004
	San Carlos	10.7	0.5	0.00028	0.00004	-	-	-	0.00059	0.00007
G5	Glass	48400	4900	-	-	47816	1.94	2.91	-	-
	Olivine	23	11	0.0005	0.0002	-	-	-	0.0012	0.0006
G7	Glass	46300	4600	-	-	48544	1.92	2.71	-	-
	Olivine	23	2	0.00049	0.00007	-	-	-	0.0012	0.0002
M7	Glass	31500	4000	-	-	32718	1.71	1.44	-	-

This is the peer-reviewed, final accepted version for American Mineralogist, published by the Mineralogical Society of America.
The published version is subject to change. Cite as Authors (Year) Title. American Mineralogist, in press.
DOI: https://doi.org/10.2138/am-2025-9738. http://www.minsocam.org/

	Olivine	23	7	0.0007	0.0002	-	-	-	0.0013	0.0004
M8	Glass	20100	2000	-	-	21981	1.37	0.64	-	-
	Olivine	13	4	0.00066	0.00022	-	-	-	0.0010	0.0003
M11	Glass	10200	1000	-	-	14548	0.86	0.16	-	-
	Olivine	9	2	0.0009	0.0002	-	-	-	0.0011	0.0003
M23	Glass	7500	800	-	-	8419	0.67	0.08	-	-
	Olivine	9	2	0.0011	0.0003	-	-	-	0.0013	0.0003

Table 4) Summary of the H_2O_T contents of run products and predicted glass H_2O_T from the models of Moore et al. and VolatileCalc

(continued…)

		SIMS		$D_{H_2O_T}^{ol/melt}$		Moore et al. (1998)	Calculated OH and H_2Om		$D_{OH}^{ol/melt}$	
	Phase	H_2O_T (µg/g)	Unc.[1]		Unc.	H_2O_T (µg/g)	OH	H_2Om		Phase
	Melt									
PSM	Inclusion	25300	2500	-	-	-	1.55	0.98	-	-
	Olivine	13	3	0.00053	0.00014	-	-	-	0.0009	0.0002

Raw SC	San Carlos	2.2	0.2	-	-	-	-	-	-	-
B-07 SC	San Carlos	3.8	0.4	-	-	-	-	-	-	-
B-14SC	San Carlos	2.6	0.3	-	-	-	-	-	-	-

*No major element data (see "Results"), so compositions were assumed to be identical to B-13

[1]Uncertainty reported as the larger value between 1 standard deviation from the mean and the long-term reproducibility of the analyses (10%; see "Results").

1128

1129

1130

This is the peer-reviewed, final accepted version for American Mineralogist, published by the Mineralogical Society of America.
The published version is subject to change. Cite as Authors (Year) Title. American Mineralogist, in press.
DOI: https://doi.org/10.2138/am-2025-9738. http://www.minsocam.org/

Revision 1

Figures

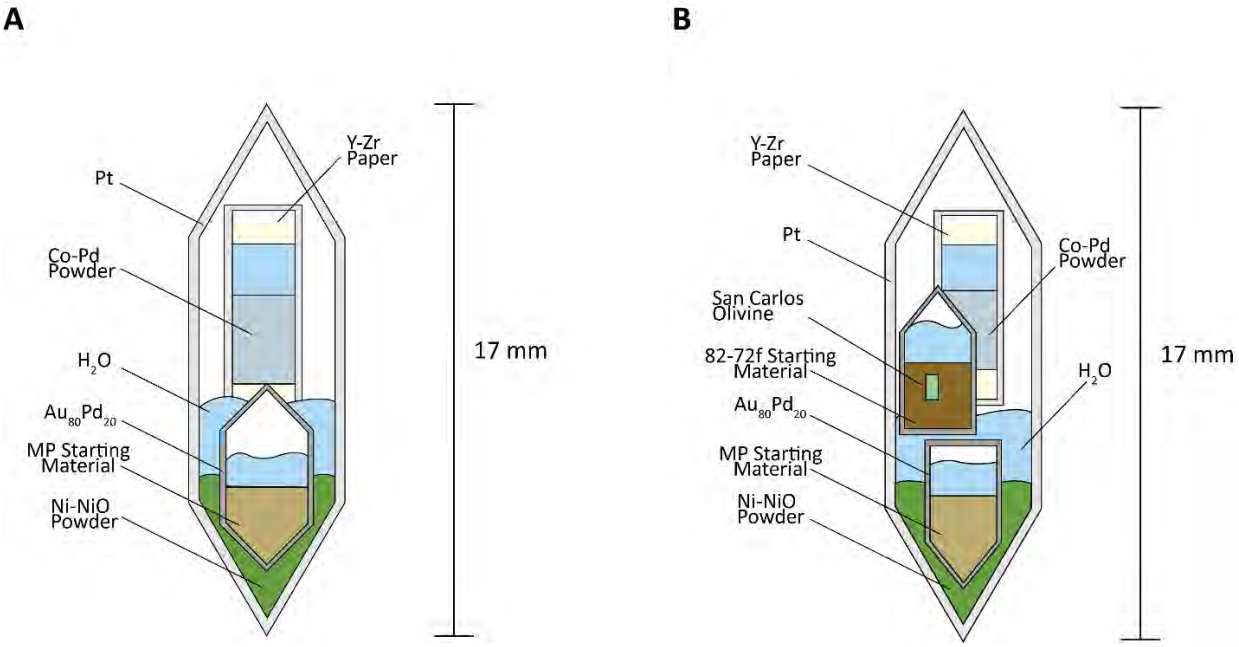

Fig. 1

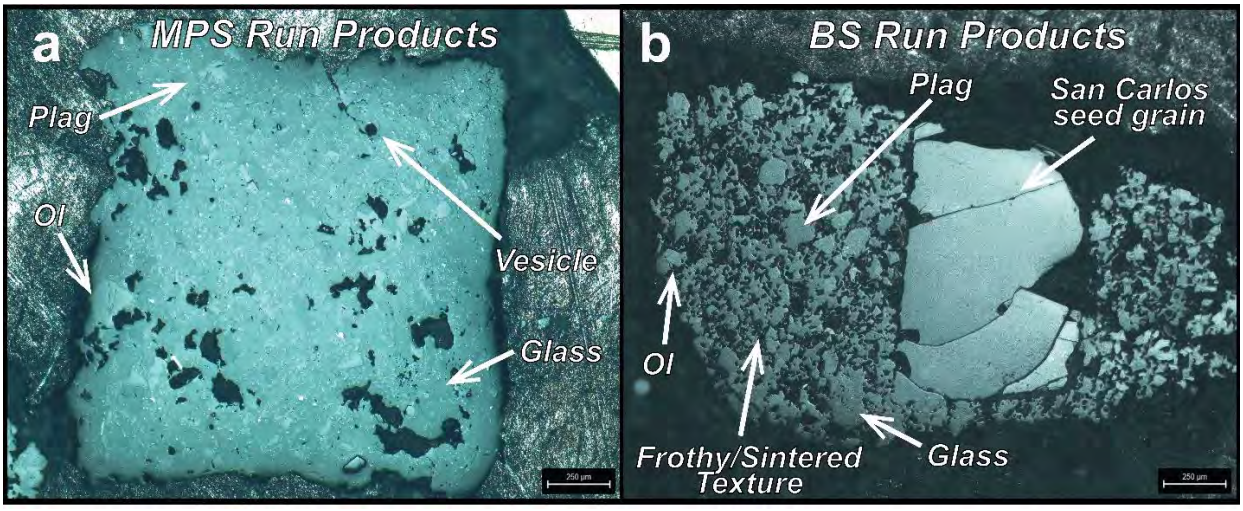

Fig. 2

This is the peer-reviewed, final accepted version for American Mineralogist, published by the Mineralogical Society of America.
The published version is subject to change. Cite as Authors (Year) Title. American Mineralogist, in press.
DOI: https://doi.org/10.2138/am-2025-9738. http://www.minsocam.org/

Revision 1

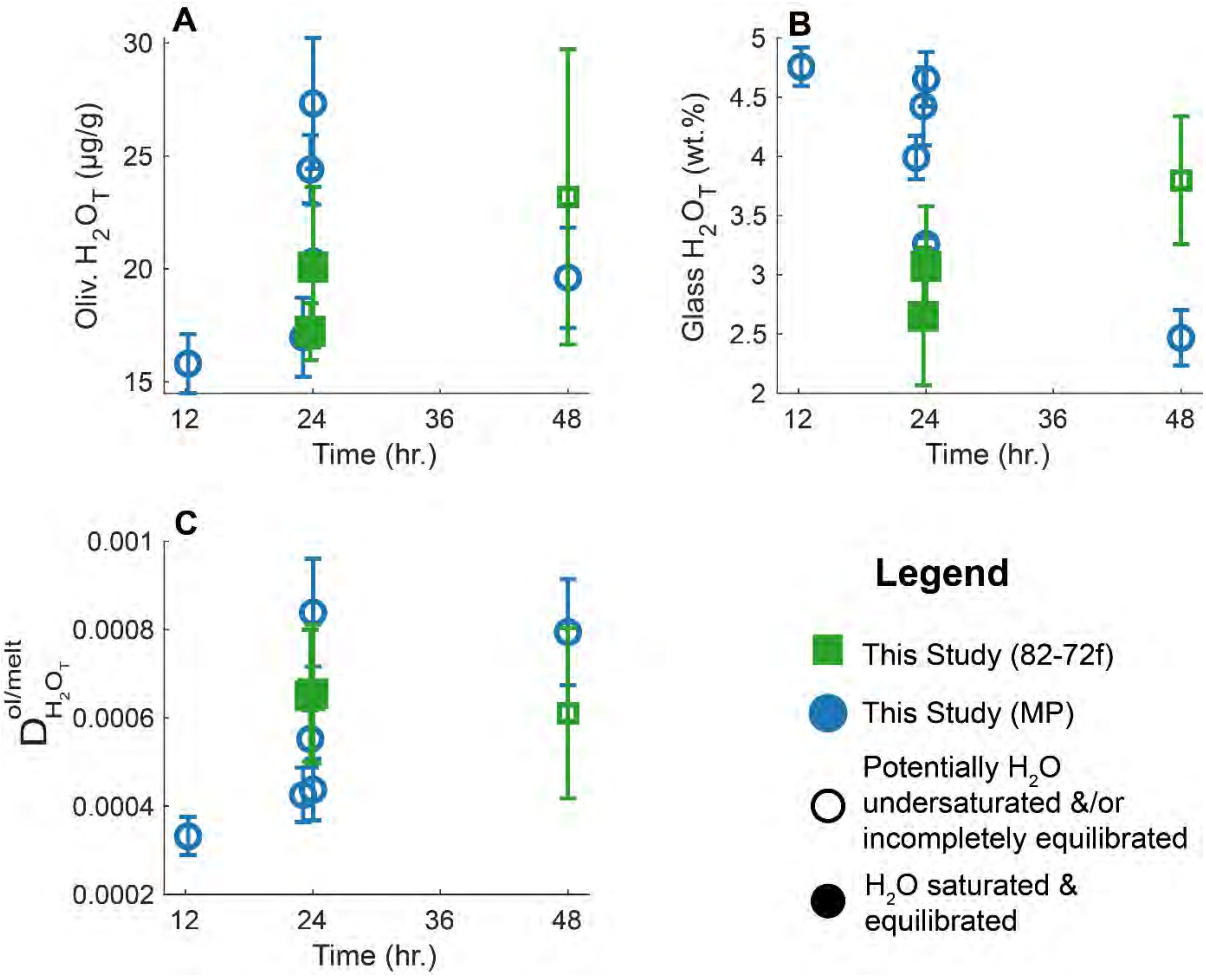

Fig. 3

This is the peer-reviewed, final accepted version for American Mineralogist, published by the Mineralogical Society of America.
The published version is subject to change. Cite as Authors (Year) Title. American Mineralogist, in press.
DOI: https://doi.org/10.2138/am-2025-9738. http://www.minsocam.org/

Revision 1

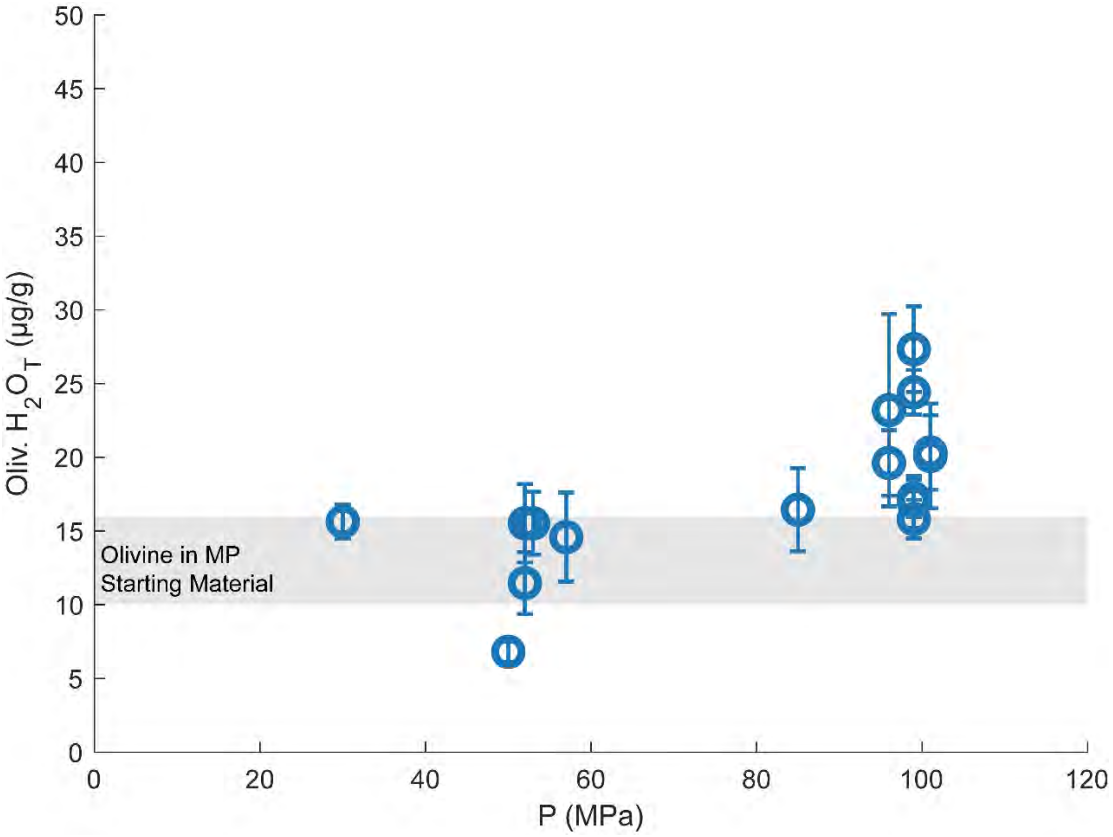

1139

1140 **Fig. 4**

This is the peer-reviewed, final accepted version for American Mineralogist, published by the Mineralogical Society of America.
The published version is subject to change. Cite as Authors (Year) Title. American Mineralogist, in press.
DOI: https://doi.org/10.2138/am-2025-9738. http://www.minsocam.org/

Revision 1

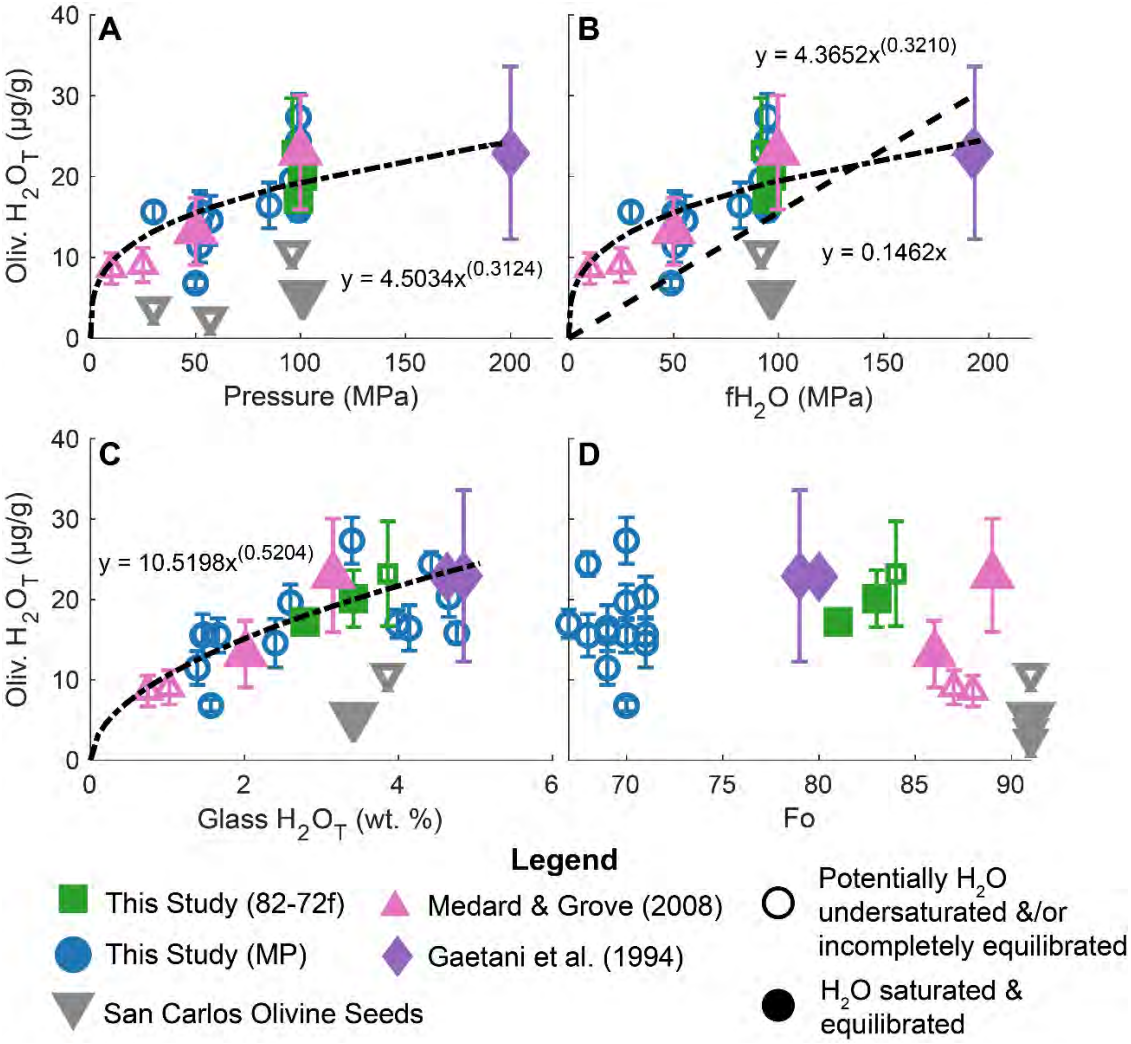

Fig. 5

This is the peer-reviewed, final accepted version for American Mineralogist, published by the Mineralogical Society of America.
The published version is subject to change. Cite as Authors (Year) Title. American Mineralogist, in press.
DOI: https://doi.org/10.2138/am-2025-9738. http://www.minsocam.org/

Revision 1

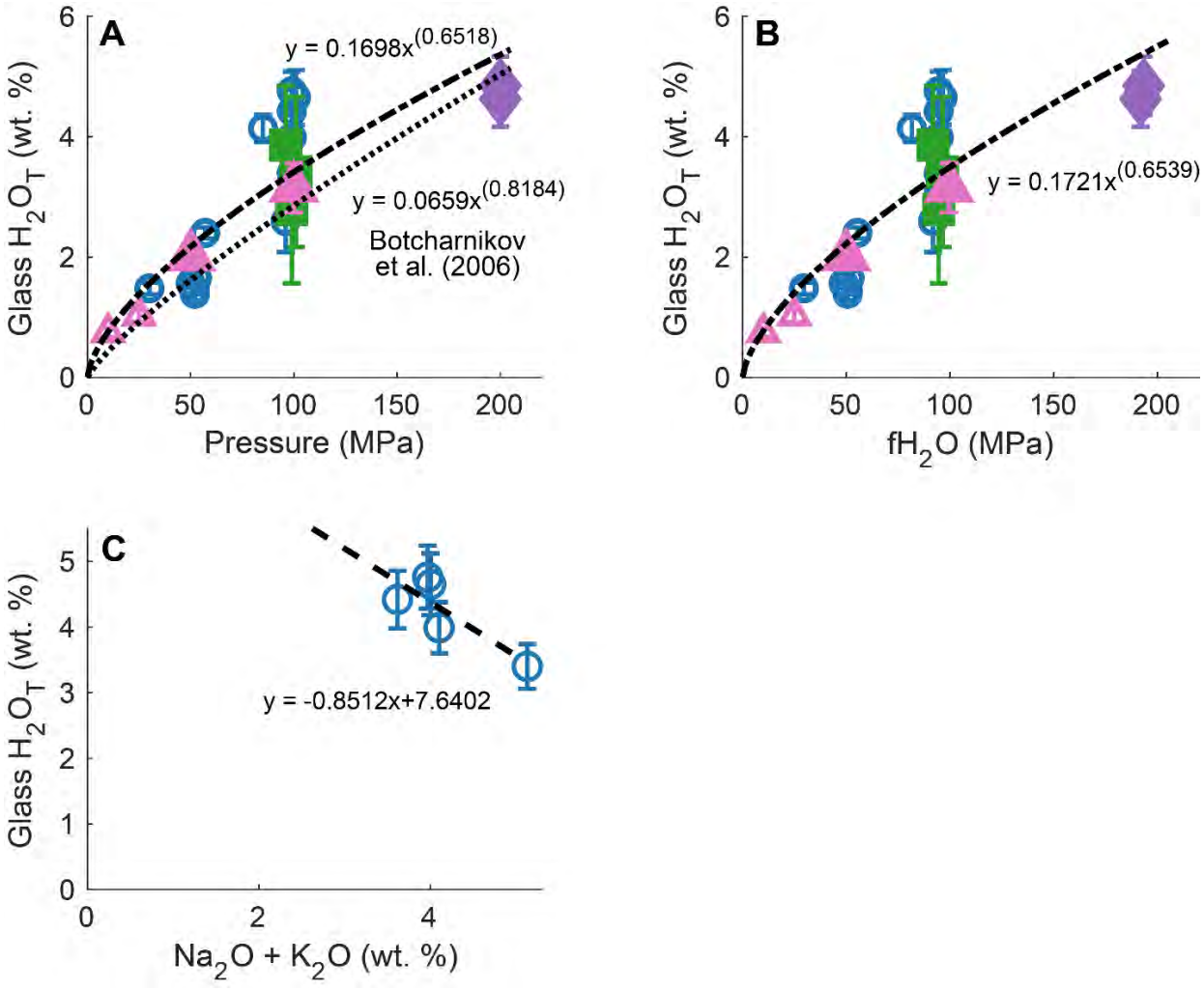

Fig. 6

This is the peer-reviewed, final accepted version for American Mineralogist, published by the Mineralogical Society of America.
The published version is subject to change. Cite as Authors (Year) Title. American Mineralogist, in press.
DOI: https://doi.org/10.2138/am-2025-9738. http://www.minsocam.org/

Revision 1

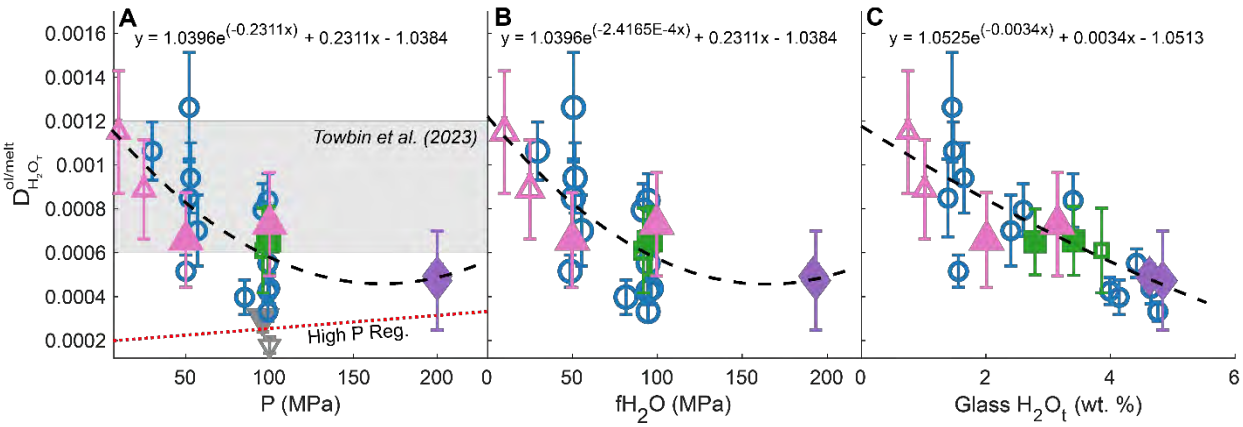

Fig. 7

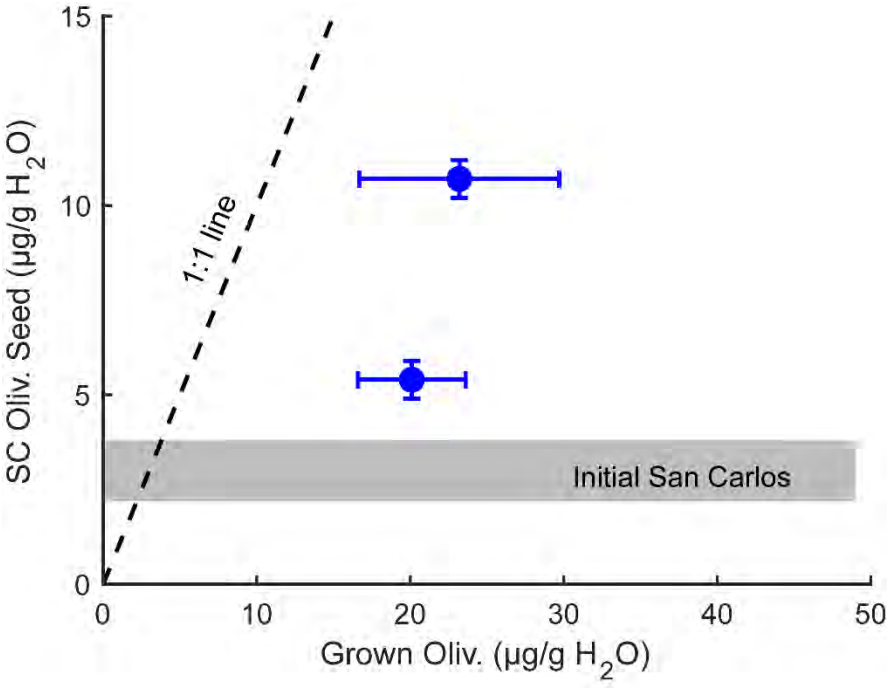

Fig. 8

This is the peer-reviewed, final accepted version for American Mineralogist, published by the Mineralogical Society of America.
The published version is subject to change. Cite as Authors (Year) Title. American Mineralogist, in press.
DOI: https://doi.org/10.2138/am-2025-9738. http://www.minsocam.org/

Revision 1

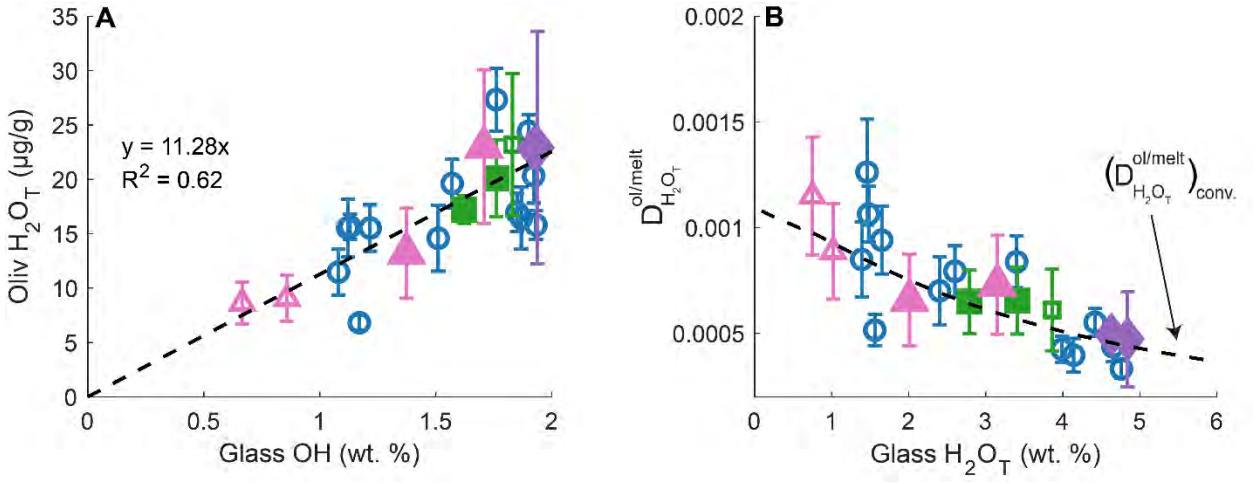

1152

1153 **Fig. 9**

1154

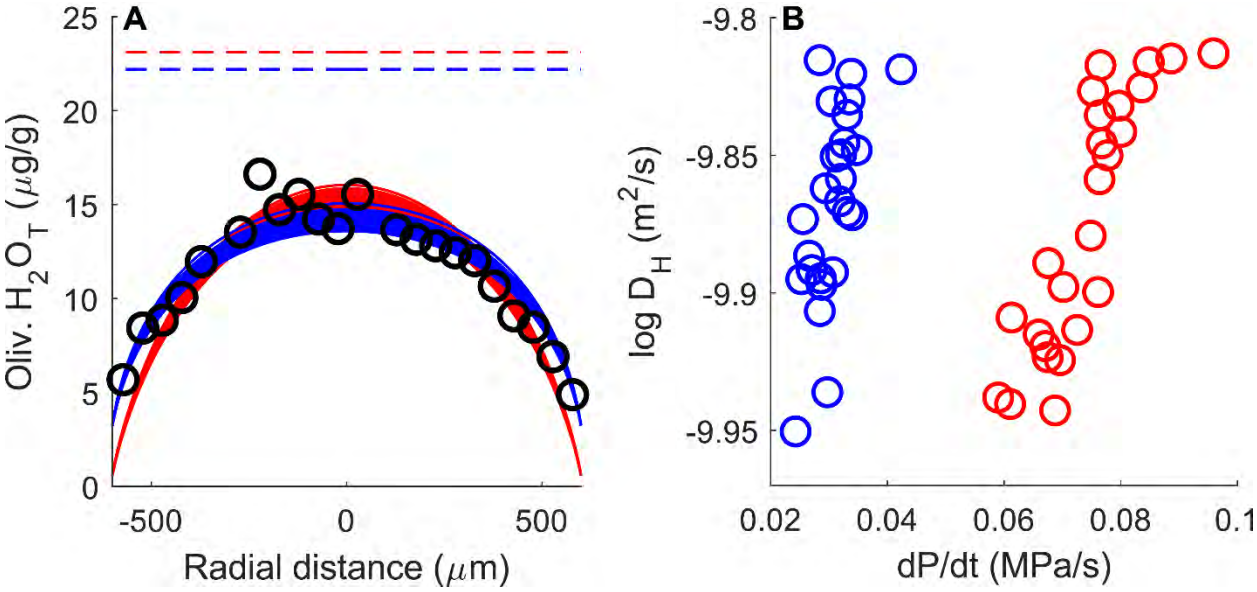

1155

1156 **Fig. 10**

1157